IOP Publishing and International Atomic Energy Agency Nuclear Fusion

Nucl. Fusion **51** (2011) 094011 (18pp) doi:10.1088/0029-5515/51/9/094011

Overview of physics results from NSTX

R. Raman[1], J-W. Ahn[2], J.P. Allain[3], R. Andre[4], R. Bastasz[5], D. Battaglia[2], P. Beiersdorfer[6], M. Bell[4], R. Bell[4], E. Belova[4], J. Berkery[7], R. Betti[4,8], J. Bialek[7], T. Bigelow[2], M. Bitter[4], J. Boedo[9], P. Bonoli[10], A. Boozer[7], A. Bortolon[11], D. Brennan[12], J. Breslau[4], R. Buttery[13], J. Canik[2], G. Caravelli[14], C. Chang[15], N.A. Crocker[16], D. Darrow[4], W. Davis[4], L. Delgado-Aparicio[4], A. Diallo[4], S. Ding[17], D. D'Ippolito[18], C. Domier[11], W. Dorland[19], S. Ethier[4], T. Evans[13], J. Ferron[13], M. Finkenthal[14], J. Foley[20], R. Fonck[21], R. Frazin[22], E. Fredrickson [4], G. Fu[4], D. Gates[4], S. Gerhardt[4], A. Glasser[1], N. Gorelenkov[4], T. Gray[2], Y. Guo[17], W. Guttenfelder[4], T. Hahm[4], R. Harvey[23], A. Hassanein[3], W. Heidbrink[24], K. Hill[4], Y. Hirooka[25], E.B. Hooper[6], J. Hosea[4], B. Hu[8], D. Humphreys[13], K. Indireshkumar[4], F. Jaeger[2], T. Jarboe[1], S. Jardin[4], M. Jaworski[4], R. Kaita[4], J. Kallman[4], O. Katsuro-Hopkins[7], S. Kaye[4], C. Kessel[4], J. Kim[26], E. Kolemen[4], S. Krasheninnikov[9], S. Kubota[16], H. Kugel[4], R. La Haye[13], L. Lao[13], B. LeBlanc[4], W. Lee[26], K. Lee[11], J. Leuer[13], F. Levinton[20], Y. Liang[11], D. Liu[24], N. Luhmann Jr[11], R. Maingi[2], R. Majeski[4], J. Manickam[4], D. Mansfield[4], R. Maqueda[20], E. Mazzucato[4], A. McLean[2], D. McCune[4], B. McGeehan[27], G. McKee[21], S. Medley[4], J. Menard[4], M. Menon[28], H. Meyer[29], D. Mikkelsen[4], G. Miloshevsky[3], D. Mueller[4], T. Munsat[30], J. Myra[18], B. Nelson[1], N. Nishino[31], R. Nygren[5], M. Ono[4], T. Osborne[13], H. Park[26], J. Park[4], S. Paul[4], W. Peebles[16], B. Penaflor[13], C. Phillips[4], A. Pigarov[9], M. Podesta[4], J. Preinhaelter[32], Y. Ren[4], H. Reimerdes[7], G. Rewoldt[4], P. Ross[4], C. Rowley[4], E. Ruskov[24], D. Russell[18], D. Ruzic[22], P. Ryan[2], S.A. Sabbagh[7], M. Schaffer[13], E. Schuster[33], F. Scotti[4], K. Shaing[21], V. Shevchenko[29], K. Shinohara[34], V. Sizyuk[3], C.H. Skinner[4], A. Smirnov[23], D. Smith[21], P. Snyder[13], W. Solomon[4], A. Sontag[2], V. Soukhanovskii[6], T. Stoltzfus-Dueck[4], D. Stotler[4], B. Stratton[4], D. Stutman[14], H. Takahashi[4], Y. Takase[35], N. Tamura[25], X. Tang[36], C.N. Taylor[3], G. Taylor[4], C. Taylor[3], K. Tritz[14], D. Tsarouhas[3], M. Umansky[6], J. Urban[32], M. Walker[13], W. Wampler[5], W. Wang[4], J. Whaley[5], R. White[4], J. Wilgen[2], R. Wilson[4], K.L. Wong[4], J. Wright[10], Z. Xia[11], D. Youchison[5], G. Yu[9], H. Yuh[20], L. Zakharov[4], D. Zemlyanov[3], G. Zimmer[4] and S.J. Zweben[4]

[1] University of Washington, Seattle, WA 98195, USA
[2] Oak Ridge National Laboratory, Oak Ridge, TN 37831, USA
[3] Purdue University, West Lafayette, IN 47907, USA
[4] Princeton Plasma Physics Laboratory, PO Box 451, Princeton, NJ 08543 USA
[5] Sandia National Laboratory, Albuquerque, NM 87185, USA
[6] Lawrence Livermore National Laboratory, Livermore, CA 94551, USA
[7] Columbia University, New York, NY 10027, USA
[8] University of Rochester, Rochester, NY 14623, USA
[9] University of California at San Diego, San Diego, CA 92093, USA
[10] Massachusetts Institute of Technology, Cambridge, MA 02139, USA
[11] University of California at Davis, Davis, CA 95616, USA
[12] University of Tulsa, Tulsa, OK 74104, USA
[13] General Atomics, San Diego, CA 92186, USA

[14] Johns Hopkins University, Baltimore, MD 21218, USA
[15] New York University, New York, NY 10012, USA
[16] University of California at Los Angeles, Los Angeles, CA 90095, USA
[17] Academia Sinica Institute of Plasma Physics, Hefei, Anhui 230031, People's Republic of China
[18] Lodestar Research Corporation, Boulder, CO 80301, USA
[19] University of Maryland, College Park, MD 20742, USA
[20] Nova Photonics, Inc., Princeton, NJ 08543, USA
[21] University of Wisconsin-Madison, Madison, WI 53706, USA
[22] University of Illinois at Urbana-Champaign, Urbana, IL 61820, USA
[23] CompX, 12808 Via Latina, Del Mar, CA 92014, USA
[24] University of California at Irvine, Irvine, CA 92697, USA
[25] National Institute for Fusion Science, Oroshi, Toki, Gifu 509-5292, Japan
[26] Pohang University of Science and Technology (POSTECH), Pohang, Gyungbuk, Korea
[27] Dickinson College, Carlisle, PA 17013, USA
[28] Think Tank Inc., Silver Springs, MD 20910, USA
[29] UK Atomic Energy Agency, Culham Science Center, Abingdon, Oxfordshire, OX14 3DB, UK
[30] University of Colorado at Boulder, Boulder, CO 80301, USA
[31] Hiroshima University, Hiroshima 739-0046, Japan
[32] Institute of Plasma Physics, AS CR, Praha 8, Czech Republic
[33] Lehigh University, Bethlehem, PA 18015, USA
[34] Japan Atomic Energy Agency, Naka, Ibaraki, Tokaimura, Japan
[35] University of Tokyo, Kashiwa, Chiba 2778561, Japan
[36] Los Alamos National Laboratory, Los Alamos, NM 87544, USA

Received 11 January 2011, accepted for publication 12 July 2011
Published 31 August 2011
Online at stacks.iop.org/NF/51/094011

Abstract
In the last two experimental campaigns, the low aspect ratio NSTX has explored physics issues critical to both toroidal confinement physics and ITER. Experiments have made extensive use of lithium coatings for wall conditioning, correction of non-axisymmetric field errors and control of $n = 1$ resistive wall modes (RWMs) to produce high-performance neutral-beam heated discharges extending to 1.7 s in duration with non-inductive current fractions up to 0.7. The RWM control coils have been used to trigger repetitive ELMs with high reliability, and they have also contributed to an improved understanding of both neoclassical tearing mode and RWM stabilization physics, including the interplay between rotation and kinetic effects on stability. High harmonic fast wave (HHFW) heating has produced plasmas with central electron temperatures exceeding 6 keV. The HHFW heating was used to show that there was a 20–40% higher power threshold for the L–H transition for helium than for deuterium plasmas. A new diagnostic showed a depletion of the fast-ion density profile over a broad spatial region as a result of toroidicity-induced Alfvén eigenmodes (TAEs) and energetic-particle modes (EPMs) bursts. In addition, it was observed that other modes (e.g. global Alfvén eigenmodes) can trigger TAE and EPM bursts, suggesting that fast ions are redistributed by high-frequency AEs. The momentum pinch velocity determined by a perturbative technique decreased as the collisionality was reduced, although the pinch to diffusion ratio, $V_{\mathrm{pinch}}/\chi_\phi$, remained approximately constant. The mechanisms of deuterium retention by graphite and lithium-coated graphite plasma-facing components have been investigated. To reduce divertor heat flux, a novel divertor configuration, the 'snowflake' divertor, was tested in NSTX and many beneficial aspects were found. A reduction in the required central solenoid flux has been realized in NSTX when discharges initiated by coaxial helicity injection were ramped in current using induction. The resulting plasmas have characteristics needed to meet the objectives of the non-inductive start-up and ramp-up program of NSTX.

1. Introduction

The National Spherical Torus Experiment (NSTX) produces plasmas with toroidal aspect ratio, that is, the ratio of the plasma major radius to its minor radius, as low as 1.25. These plasmas can be heated by up to 6 MW radio-frequency (RF) waves and 7 MW of deuterium neutral-beam injection (NBI). The plasmas in NSTX are surrounded by closely fitting conducting plates to inhibit the development of instabilities driven by the plasma pressure. The poloidal field coils provide flexible plasma shaping and a set of six non-axisymmetric external coils provide for correction of field errors and feedback control of some plasma instabilities. Results from the six basic science topical groups in NSTX are covered in the following sections: (2) macrostability physics, (3) transport and turbulence physics, (4) boundary physics and lithium research, (5) waves and fast particle physics, (6) solenoid free start-up and (7) advanced scenarios and control.

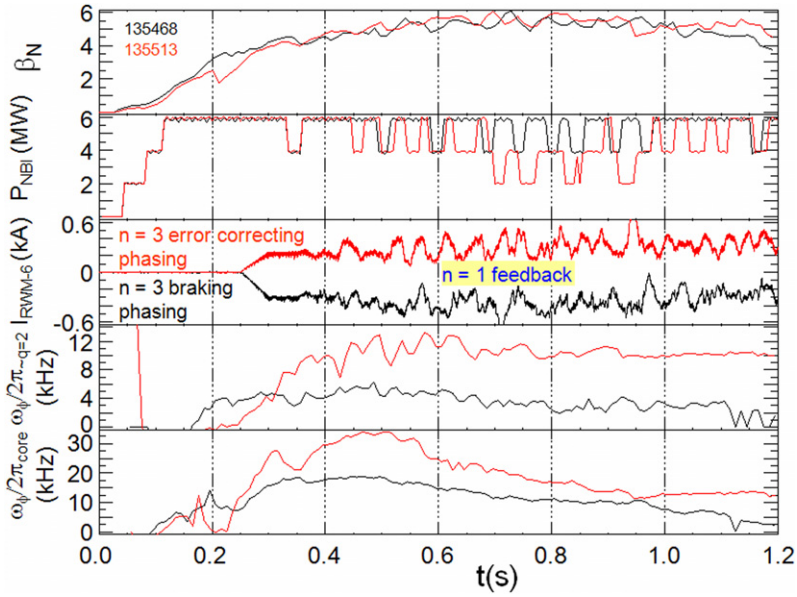

Figure 1. Comparison of two discharges in which β_N control was used while the plasma rotation was varied. The black traces are for a discharge where the RWM coils were used to apply an $n = 3$ braking pulse to slow down the plasma rotation, while for the red traces, $n = 3$ fields are applied to reduce the intrinsic error. For both discharges, $n = 1$ RWM feedback control is used. The top panel shows β_N well controlled for both discharges. The second panel shows the modulations in the neutral-beam waveform under feedback control to maintain the requested β_N. The third panel shows the current in one of the error-correction coils. The lowest two panels show the plasma rotation frequency at the $q = 2$ surface and at the axis. The rotation was substantially reduced by the $n = 3$ braking. The discharge with higher rotation requires less neutral-beam power to maintain the same β_N.

Research conducted in support of ITER and the sections in which they are located are resistive wall mode (RWM) studies (2.1), error-field studies (2.3), neoclassical tearing modes (NTMs) (2.4), ELM pacing studies (2.5), L–H threshold studies (3.1), momentum pinch velocity dependence on collisionality (3.2), divertor heat load studies (4.1) and instabilities associated with fast-ion transport (5.2).

2. Macrostability physics

2.1. RWM control physics and beta feedback control at varied rotation

NSTX routinely operates with normalized-beta, $\beta_N = \beta_T/(I_p/aB_T)$ (units of % m T/MA) substantially above the $n = 1$ no-wall ideal stability limit. These plasmas are susceptible to the growth of RWMs unless stabilizing plasma rotation profiles can be maintained. Since operation at steady, high β_N is desirable, combined $n = 1$ RWM control and feedback control on β_N has been implemented in NSTX. This has been achieved at different plasma rotation levels, as shown in figure 1 [1]. High pulse-averaged β_N is maintained with reduced levels of β_N fluctuation. The NBI power is feedback controlled to maintain constant β_N, but not plasma rotation. Despite this, the toroidal rotation in the outer plasma reaches approximate steady state in these plasmas through an interesting interplay of effects. Specifically, increasing NBI heating increases the drive torque for plasma rotation, as well as increasing plasma β_N and T_i. The higher β_N increases the plasma amplification of the applied field. The combination of the amplified error field and the higher T_i increases the neoclassical toroidal viscosity braking torque [2]. Thus, as the NBI power varies, the changes in the driving and braking torques tend to offset each other, producing almost steady plasma rotation.

The RWM control coils are also routinely used to compensate an intrinsic, slowly varying $n = 3$ field error [3]. This improves plasma performance by allowing steady and rapid toroidal rotation. Experiments confirmed that the observed $n = 3$ error field is due to non-circularity in the main vertical field coil [4], and an improved correction scheme was found. Improved compensation of the RWM sensor for direct pickup of the control fields and a term proportional to the product of the OH and TF coil currents has been particularly important for optimizing the $n = 1$ and $n = 3$ error-field control. In controlled experiments, favourable feedback phase and gain settings were found for both the poloidal and radial field RWM sensor arrays (48 coils total). The RWM B_R sensor feedback phase for optimal suppression agrees with theory, and these sensors are now routinely used. Dedicated experiments have been very successful in stabilizing long-pulse plasmas with ratios of β_N/l_i between 12 and 13, whereas equivalent plasmas previously produced without this optimization suffered frequent RWM-induced disruptions.

An advanced RWM state-space controller was recently implemented that uses a reduced order model of the 3D conducting structure of NSTX and a high-beta $n = 1$ ideal plasma instability eigenfunction [5]. Such a controller has been proposed for RWM stabilization in ITER, since it has the potential to improve RWM control with coils placed further from the plasma and partially shielded by conducting structures. In initial experiments, large resonant field amplification (RFA) causing plasma disruption was sufficiently suppressed to allow stable plasma operation. The state-space controller produced a stable, long-pulse (limited by magnet heating constraints), low internal inductance (l_i)

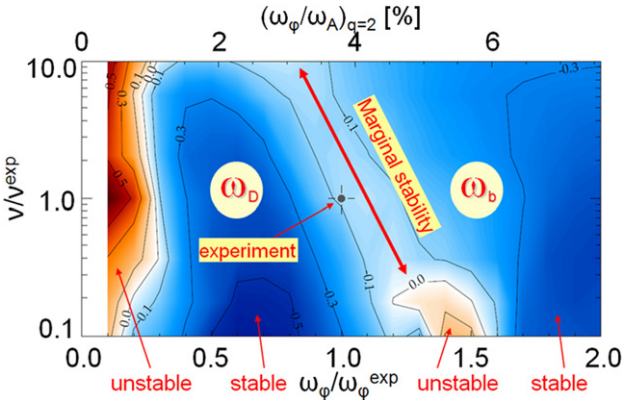

Figure 2. Contours of the calculated growth rate of the $n = 1$ RWM versus collisionality and rotation frequency, each normalized to their experimental values. Note that despite having significant plasma rotation of >0.5% of the Alfvén frequency at the $q = 2$ surface (indicated on the top axis), there are regions between the stabilizing precession drift resonance (ω_D) and the stabilizing bounce resonance (ω_b) regions where the RWM is marginally stable.

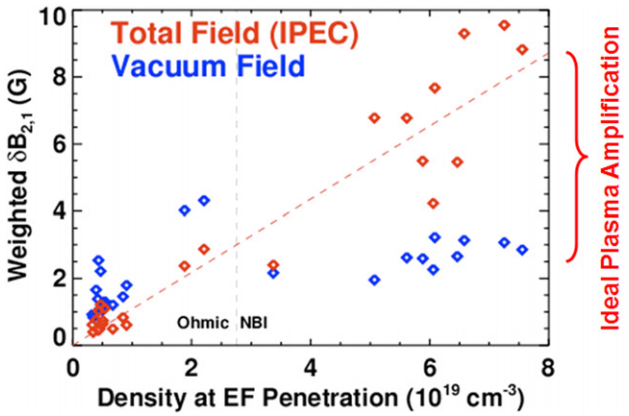

Figure 3. Inclusion of the plasma amplification of an external error field calculated by IPEC restores a linear scaling of the threshold for mode locking with plasma density which breaks down if only the external field error is considered.

plasma, β_N exceeding 6.4, and β_N/l_i exceeding 13—a record value for a stable plasma at high plasma current (I_p = 1 MA) [1].

2.2. RWM passive stabilization physics

NSTX experiments have discovered that the RWM can become unstable at intermediate levels of plasma rotation, [6] significantly greater than those reported in DIII-D [7]. Analysis has shown kinetic effects, including resonances with trapped and passing thermal ion bounce and precession drift frequencies are important for determining the plasma rotation level and profile required to stabilize the mode, as seen in figure 2. [1, 8] The calculations of the influence of fast ions on RWM stability have been performed with the MISK code [9] which computes the perturbed mode energy, including kinetic effects using the unperturbed ideal-kink eigenfunction. These calculations predict that the RWM will become progressively more stable as the fast-ion pressure is increased. To test these predictions, experiments were performed in NSTX varying the fast-ion content by varying the plasma current and field at fixed safety factor, q, to change the plasma temperature and density and, thereby, the fast-ion slowing-down time. As expected, the fast-ion content measured by the fast-ion D-alpha (FIDA) diagnostic was significantly reduced for the plasma with lower field and current. A higher plasma rotation frequency was required to achieve stability to the RWM for the plasma with lower fast-ion content, consistent with the theoretical prediction. The stabilization from energetic particles is also predicted to be nearly independent of the plasma rotation frequency because the bounce and precession drift frequencies for energetic particles are much larger than the plasma rotation frequency. Even with energetic-particle stabilization, the RWM can still be driven unstable in a band of rotation between the stabilizing precession drift and bounce resonance frequencies. Low frequency MHD spectroscopy [10] was used to directly measure RWM stability in these plasmas by examining the RFA of a low amplitude applied $n = 1$ field. Discharges at nearly constant β_N above the $n = 1$ ideal no-wall limit and with rotation profiles near marginal stability have shown greater than a factor of 2 variation in RFA as the plasma rotation is slowed.

2.3. Error-field threshold in high-beta plasmas

Magnetic field asymmetries ('error fields'), which naturally arise in the design of a tokamak, are known to be a concern in driving instabilities. At low levels these fields are shielded out by a rotating plasma, but if the fields are sufficiently large, this shielding interaction generates a torque, braking the plasma and reducing the shielding response, thereby enabling a bifurcation to a large static island. This island can greatly degrade confinement and destabilizes the plasma leading to disruption. It is therefore important to estimate the field threshold for locking and to reduce the error field below the threshold. Estimating the actual driving field at the rational surfaces has been significantly improved by employing the Ideal Perturbed Equilibrium Code (IPEC) [11], which calculates the ideal plasma response, shielding currents and the total resonant field, δB_{mn}, at the rational surfaces where $q = m/n$. At increased β_N, the applied field can be amplified and thereby become more destructive. To explore this, perturbing $n = 1$ fields were applied to the plasma with varying phases, application times and ramp rates. These scans were repeated for three target discharges designed to provide a further scan over β_N. At high β_N, using only a vacuum field calculation of the applied field, the error-field penetration occurred at significantly lower applied field than expected from previous scaling developed for low β_N ohmic plasma [12]. However, if the effect of the plasma response in amplifying the error field at high β_N is considered, as calculated by IPEC, a linear scaling of the threshold perturbation with density is restored, as shown in figure 3. This validates the ideal response model as being a more physically correct way to represent the fields present in the plasma.

2.4. Physics of NTMs

One of the key challenges for future devices is the avoidance of tearing modes. These usually manifest as NTMs, with the amplitude of any island being driven by the helical perturbation

in the bootstrap current induced by the island itself. Studies on NSTX have focused on two key aspects of their behaviour pertinent to their extrapolation to next step devices such as ITER—the role of the physics governing the threshold mechanisms for the modes and the role of rotation.

The difference in aspect ratio between NSTX and DIII-D has enabled the aspect-ratio scaling of the marginal island width for growth of the $n = 1$ NTM to be determined. The destabilization of NTMs involves the physics of small-island threshold effects and seeding of the initial perturbation. Exploring the aspect ratio dependence of this physics tests the scaling of the mechanisms responsible for the extrapolation to larger devices such as ITER, as well as elucidating the underlying mechanisms more clearly. The physics of the small-island stabilizing terms was investigated in NSTX by generating an NTM at high beta and then reducing beta to the 'marginal point' where the small-island effects just balance the sum of the classical stability, the curvature and the helically perturbed bootstrap current. At beta below this balance point, self-stabilization of the NTM occurs. Comparison of the 'offset' conditions for the $n = 1$ NTMs between DIII-D and NSTX shows that the marginal island width generally scales with the ion banana-orbit width (proportional to $\varepsilon^{1/2} \cdot \rho_{\theta i}$, where ε is the inverse aspect ratio and $\rho_{\theta i}$ is the ion poloidal gyro-radius) at the resonant $q = m/n$ surface. Further, the data show an advantage at low aspect ratio; the stabilizing curvature effect is relatively greater, making for relatively less susceptibility to NTM excitation.

A key further challenge for future devices will arise because they are likely to have much lower rotation than present facilities. This leads to two principal mechanisms of concern for generation of performance limiting tearing modes such as the 2/1 NTM (denoted as poloidal/toroidal mode number). Firstly, lower rotating plasmas are more susceptible to error fields (small asymmetries in the magnetic fields that naturally arise in a tokamak in its design and construction) [12], which can break a resonant surface and drive tearing. Secondly, lower rotation is known to decrease the stability of tearing modes, lowering the β threshold for their onset [12]. These two effects actually combine in H-mode plasmas, where it is found that β limits for tearing modes are reduced when error fields are applied.

This physics has been elucidated on NSTX by exploring the braking mechanisms of different types of error field, and its linkage to tearing mode thresholds, described in detail in [13] and summarized here. In these experiments, β ramps were deployed to reach the 2/1 NTM β limit. In plasmas without significant error field applied, this led to a 2/1 tearing mode with high rotation, at about 6.5 kHz, due to the strong torque applied by the neutral-beam heating. However, application of error fields lowered the plasma rotation (and rotation shear), which in turn led to a decrease in NTM onset bootstrap thresholds [13]. By varying the mix of $n = 1$ and $n = 3$ fields, rotation profiles were varied enabling the effect on NTM stability to be isolated to a rotation shear correlation, rather than with rotation itself. This parameter is known to be associated with changes in underlying tearing stability [14], and thus error-field effects in H-modes can be interpreted in terms of its braking leading to changes in the stability of the NTM. This explains why application of static error fields can trigger formation of rotating modes.

During these experiments it was also found that both $n = 1$ fields (which have strongly resonant components) and $n = 3$ fields (which are almost entirely non-resonant) led to similar levels of braking, suggesting that in these high rotation discharges, both types of field may be interacting through neoclassical toroidal viscosity effects (as might be expected theoretically, as resonant couplings will be weak at high rotation). However, once rotation was braked to about half its natural level, a transition to locked mode formation (by definition a resonant process) was observed, even when non-resonant $n = 3$ fields were predominantly applied. This is interpreted as being due to the proximity of these plasmas to natural tearing instability, coupled with their decreased rotation, which is expected to lead to a heightened resonant response to any residual $n = 1$ fields (as observed on DIII-D [13]).

These results highlight the underlying physics mechanisms of the NTM and possible strategies to help raise thresholds and provide control—by changes to underlying stability through rotation shear or the current profile. It also highlights the significant role error fields can play in NTM stability, making error-field correction a key issue for standard H-mode plasmas, in addition to the previously known limits at low density (where plasma rotation can be more readily stopped) or near the ideal limit (where fields are strongly amplified by the kink instability). The braking process identified allows error-field thresholds to be considered in terms of a torque balance, even for these H-modes with rotating NTM onset, much akin to that for conventional error-field penetration.

2.5. ELM pacing with non-axisymmetric coils

In NSTX H-mode plasmas where ELMs have been suppressed by lithium conditioning, ELM pacing with periodic pulses of non-axisymmetric (typically, $n = 3$) field perturbations using the RWM coils has been shown to be effective at preventing impurity accumulation and high radiated power while retaining high confinement. As shown in figure 4, for a pacing frequency of 10 Hz the total stored energy decrement from the triggered ELMs is small, 10–15%, while the radiated power at the end of the current flat-top is reduced by a factor of 3. By increasing the triggering frequency to 30 Hz, the ELM size, expressed as the fraction of plasma energy lost at each ELM, is reduced to ~5% [15, 16]. In addition to ELM pace-making with pulsed non-axisymmetric fields, a scenario was developed for ELM pacing via vertical 'jogs' of the plasma [17]. As shown in figure 5, ELM pacing at 30 Hz was observed with the ELMs synchronized to the plasma vertical motion. A reduction in the ELM size with increasing jog frequency was observed. Simultaneous application of a steady-state $n = 3$ field allowed ELMs to be triggered with smaller jogs. The vertical jogs do not result in radiated power excursions; however, there is no reduction in the radiated power compared with the already ELMing reference discharge.

3. Transport and turbulence in plasmas

3.1. L–H threshold studies in support of ITER

In NSTX helium plasmas heated by deuterium NBI, it was found that the L → H threshold power normalized to the

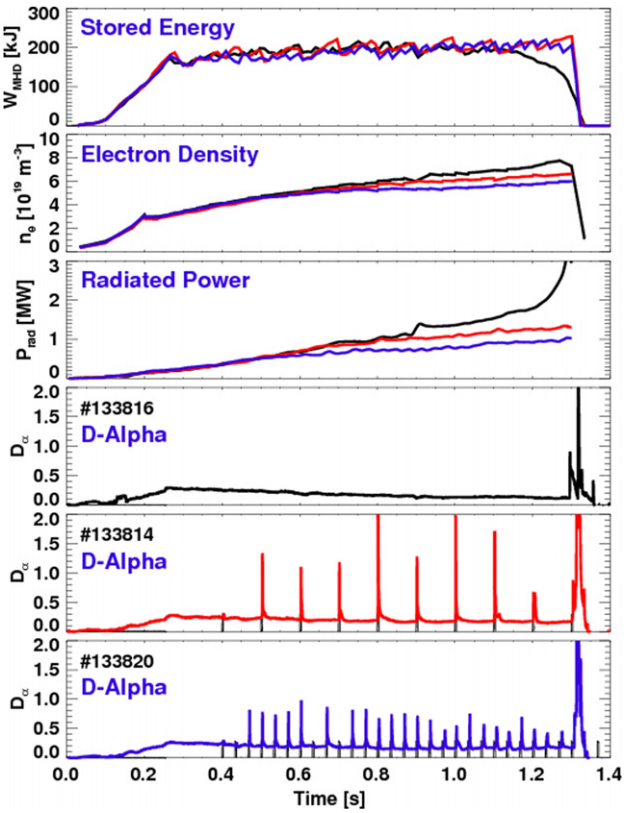

Figure 4. Comparison of parameters for an ELM-free discharge (black) and two similar discharges with ELMs triggered by pulsed $n = 3$ RMPs at 10 Hz (red) and 30 Hz (blue). Note that for shot 133816 there are no ELM signatures in the D-alpha trace. The pulses of RMP are shown by the small black spikes under the D-alpha traces which show the ELM signatures. Compared with the ELM-free case, there is a decrease in the electron density and a substantial decrease in the radiated power which increases with ELM frequency. However, the stored energy remains unaffected by the ELM triggering.

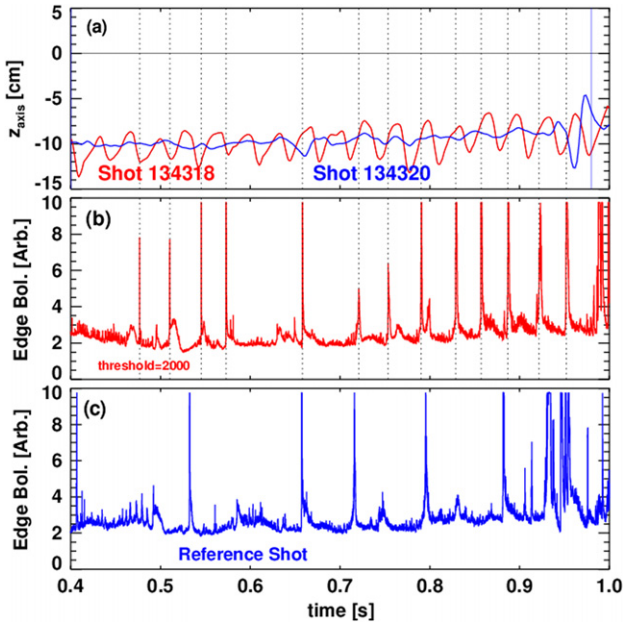

Figure 5. The blue trace (frame (c)) shows ELM signatures from a reference ELMy discharge. The corresponding red trace (frame (b)) shows increased ELM signatures in a discharge that was subjected to vertical up-down motion of the plasma column. Frame (a) (red trace) shows that the Z-axis of the plasma for this discharge is at about $Z = -10$ cm and the plasma undergoes a ± 2 cm vertical oscillation.

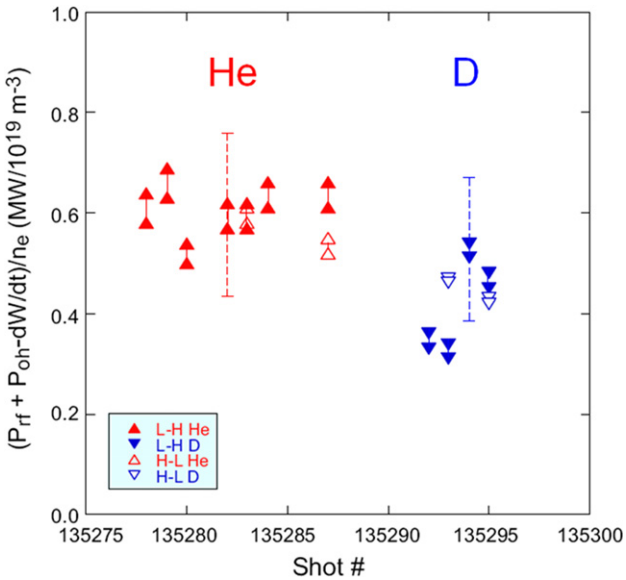

Figure 6. The density-normalized L → H and H → L power threshold versus shot number for an experiment in which ramped HHFW heating power was used to trigger H-mode transitions in helium (red) and deuterium (blue) plasmas. The normalized L → H threshold power is 20–40% higher for helium discharges than deuterium discharges.

plasma density, $P_{\mathrm{LH}}/n_{\mathrm{e}}$, was about 20–40% higher in helium plasmas than in deuterium plasmas, as shown in figure 6. This suggests that operation in helium may be a better approach to developing H-mode scenarios in the early non-nuclear phase of ITER operation when the heating power will be limited, since results from other experiments have shown that hydrogen plasmas have threshold powers nearly twice that for deuterium.

Other experiments were performed to measure the dependence of the L→H threshold on applied non-axisymmetric fields. It was found that $P_{\mathrm{LH}}/n_{\mathrm{e}}$ is significantly, up to 65%, higher with an applied $n = 3$ field. Consistent with earlier comparisons of the threshold between plasmas with very different toroidal rotation produced by high harmonic fast wave (HHFW) and NBI heating, the difference in the rotation produced by the applied perturbation did not appear to be the dominant factor. It was also found that $P_{\mathrm{LH}}/n_{\mathrm{e}}$ was almost a factor of 2 higher for 1 MA plasma current than for 0.7 MA, indicating a strong dependence on plasma current. As shown in figure 7, calculations with the code XGC-O [18] suggest that this is due to reduced radial electric field shear for the higher current discharge in the region where the pedestal forms after the transition.

Motivated by recent calculations with the XGC-O code [19] suggesting a strong dependence on the plasma triangularity at low aspect ratio, an experiment was conducted to measure the L → H power threshold for two different triangularities (δ) at roughly constant X-point height. The power threshold was 20–30% lower at the lower δ, qualitatively consistent with the XGC-O calculations of a larger radial

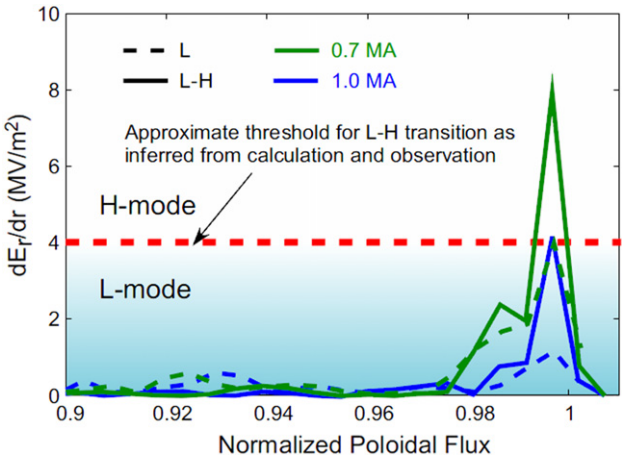

Figure 7. XGC-O code calculations of the radial electric field gradient suggest that the increased L → H power threshold at higher plasma current is attributable to reduced radial electric field shear. The green and blue dashed traces are for discharges that remain in L-mode. The solid green trace is the profile for the 0.7 MA discharge and the solid blue line is for the 1 MA discharge. The data suggest that there is a threshold radial electric field shear, indicated by the red dashed line, in the region where the pedestal forms below which a discharge will remain in L-mode.

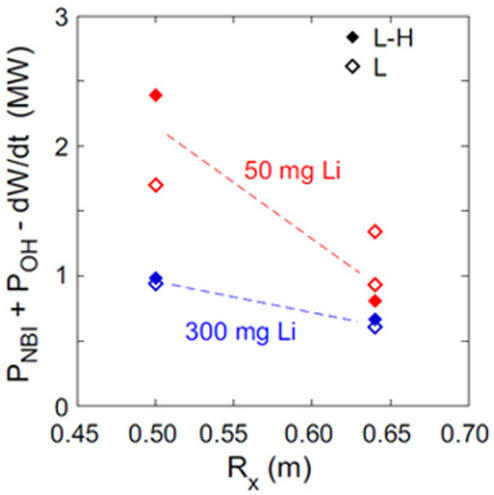

Figure 8. The L → H power threshold decreases as the X-point radius is moved to larger radii. There is a further decrease with increased lithium deposition on the lower divertor plates. The absolute density corresponding to the 2.4 MW case is 3.0×10^{19} m^{-3} and that for the 1.4 MW case is 2.3×10^{19} m^{-3}.

electric field and gradient at low δ. The primary parameter appears to be the lower toroidal field at the larger radius X-point of the lower δ discharge (figure 8).

As also shown in figure 8, lithium coating of the plasma-facing components (PFCs) using evaporators aimed at the lower divertor (see section 4.3) was found to reduce the power threshold in NBI-heated plasmas from 2.7 MW without lithium to 1.4 MW with lithium applied, corresponding to a reduction in $P_{\rm LH}/n_{\rm e}$ by $\sim$ 30% from 0.9 to 0.6 MW/10^{19} m^{-3}.

In experiments with the toroidal magnetic field (TF) reversed (the plasma current direction remaining unchanged) so that the $B \times \nabla B$ particle drift for the ions changed from being towards the lower divertor to being towards the upper divertor, it was found that the L→H threshold in the loss power ($P_{\rm loss} = P_{\rm OH} + P_{\rm aux} - {\rm d}W/{\rm d}t$) for upper single-null discharges was lower by about 40% than for lower single null discharges. Furthermore, when lithium was used to coat the *lower* divertor, this reduction in threshold power for the *upper* single-null plasmas approximately doubled compared with that for the lower single null discharge (the threshold power was 1.4 MW for the LSN versus 0.5 MW for the USN discharge), confirming the large impact lithium has in reducing the threshold power.

3.2. Dependence of momentum pinch velocity on collisionality

Recent theory has suggested a relatively weak dependence of the momentum pinch on collisionality. It is critical to validate this, since a degradation of this pinch at low collisionality would be unfavourable for achieving peaked rotation profiles in future burning-plasma devices such as ITER, which will have small external momentum input. In NSTX, the braking torque from the application of non-resonant magnetic perturbations was used to modify the gradient in the toroidal velocity differently from the change in the velocity itself. The diffusive and pinch contributions to the transport were then inferred from measured rotation data by modelling the toroidal angular momentum flow through each radius using the momentum source from the NBI calculated by TRANSP. A non-linear least-squares fit was used to determine an assumed time-independent momentum diffusivity χ_ϕ and a momentum pinch velocity $V_{\rm pinch}$ that best reproduced the time history of the toroidal angular momentum profile. In a series of discharges, the collisionality was varied while maintaining other dimensionless quantities as close to constant as possible. As shown in figure 9, in general, the inward pinch velocity in both NSTX and DIII-D was found to decrease as the collisionality is reduced, suggesting that there is commonality in the mechanisms responsible for the momentum pinch at both low and conventional aspect ratio [20]. In terms of peaking, the rotation profile, the ratio of the pinch to the momentum diffusivity is more important than the absolute pinch velocity. This shows a weak dependence on collisionality [20].

3.3. Electron thermal transport

Previous experiments [21] identified a correlation between fast particle modes identified as global Alfvén eigenmodes (GAEs) and increased electron thermal transport in the core of NSTX plasmas. In a recent study, the neutral-beam power was varied to modify the character and amplitude of the GAE activity in H-mode discharges. A key feature of this experiment was the availability of inteferometric measurements from the high-k scattering diagnostic [22]. Fluctuations in the line-integrated density were measured at a tangency radius of $\sim$115 cm, near the predicted peak of the GAE mode structure, and at a tangency radius of $\sim$120 cm, where the GAE mode amplitude is predicted to be lower by an order of magnitude.

The electron transport increased with the level of GAE activity. However, for $r/a < 0.5$, calculations of the transport based on the measured density fluctuations from interferometric measurements have fallen short of the experimental values of $\chi_{\rm e}$ by factors of 4–10. Further analysis of the GAE measurements using high-frequency magnetic pickup coils has revealed a 'bursting' character of the modes so

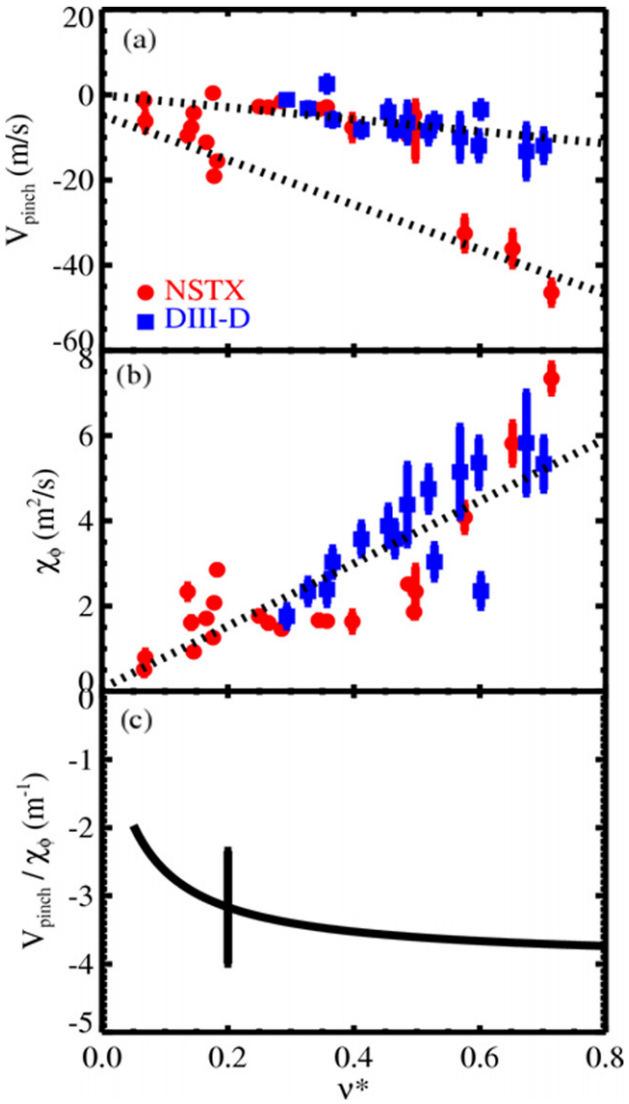

Figure 9. Variation with electron collisionality, ν^*, for NSTX and DIII-D in (*a*) the momentum pinch velocity and (*b*) the momentum diffusivity. Panel (*c*) shows the ratio of the momentum diffusivity to the pinch velocity for the indicated fits to the data from both machines.

that the peak magnitude of the GAE density fluctuations may be far higher than the time-averaged values used in the transport calculations (figure 10(*a*)). Numerical calculations show that the GAE-induced thermal diffusivity χ_e can scale strongly with mode amplitude α, varying as $\chi_e \propto \alpha^{(3-6)}$, (figure 10(*b*)) as the modes begin to overlap, leading to stochastic transport, which indicates that under some circumstances the peak mode amplitude can strongly dominate the electron transport for larger GAE amplitudes and be the dominant mechanism for the observed anomalous thermal transport.

In NSTX, electron gyro-scale density turbulence is studied using tangential 280 GHz microwave scattering ('high-*k*' scattering) diagnostic [23]. The high-*k* scattering system samples a 1D k_r spectrum in the 2D $k_\perp$ space (where $k_\perp$ denotes wavenumber perpendicular to the magnetic field). The system has five channels, now capable of covering k_r from 5 to 20 cm^{-1} with a resolution of 0.7 cm^{-1}. Over the range of k_r previously accessible [24–26], the k_r spectra showed a monotonic power law trend with no saturation of the spectral power evident at the smallest accessible wavenumbers. This year, simultaneous measurements were made with all five channels. The data have revealed an apparent saturation of the spectral power at small wavenumbers for $k_\perp\rho_s < 6$ in L-mode plasmas and for $k_\perp\rho_s < 10$ in H-mode plasmas. Figure 11(*a*) compares fluctuation levels in L-mode and H-mode plasmas with identical I_p, B_T and neutral-beam power. Although the spectra are similar for $k_\perp\rho_s > 10$, the spectral power of the H-mode plasma for $k_\perp\rho_s < 10$ saturates at a level smaller than that of the L-mode plasma by up to two orders of magnitude. This dramatic difference in spectral power between the L- and H-modes at small wavenumber is consistent with longer-wavelength electrostatic turbulence being the dominant source of the anomalous transport in the L-mode. As seen in figure 11(*b*), there is also a further dramatic decrease in the level of normalized density fluctuations for the H-mode discharges that benefitted from lithium conditioning.

3.4. Observation of improved performance regimes

A new high-performance regime, the 'enhanced pedestal' (or EP) H-mode, has been observed in NSTX discharges, where the H-mode edge 'pedestal' temperature doubles and the energy confinement increases by 50%. The transition to the EPH-mode is triggered by a large ELM, either naturally occurring or externally triggered by 3D fields. As shown in figure 12, the transport barrier grows inwards from the edge, with a doubling of both the pedestal pressure width and the spatial extent of steep radial electric field shear. The resulting discharge exhibits a 50% increase in energy confinement time, up to 1.6 to 1.7*ITER98y2 H-mode scaling, and a β_N up to 6.5 which is maintained for three energy confinement times [27].

4. Plasma boundary physics

4.1. Studies of heat fluxes in the scrape-off layer (SOL) and to the divertor surface

The peak heat flux at PFCs is intimately tied to the downstream deposition footprint on both the SOL and private-flux region sides, which in turn are related to cross-field transport and the upstream midplane profile widths. The dependence of the lower divertor heat flux profiles on P_{NBI}, I_p, B_T and lithium conditioning in H-mode discharges has been measured with IR thermography. Previously we reported that the SOL heat flux width at the discharge outboard midplane, λ_q^{mid} (i.e. the divertor profile width magnetically mapped to the midplane), decreased with I_p, and was relatively independent of P_{NBI} at high P_{NBI} for low triangularity, $\delta \approx 0.4$, discharges. Over the past two years these measurements were extended to higher triangularity. The data in figure 13 show that at $\delta \approx 0.7$, λ_q^{mid} scales as $I_p^{-1.6}$, and is largely independent of P_{NBI} and B_T [28]. In addition, when lithium coatings resulted in ELM-free discharges, there was a further contraction of λ_q^{mid} by about 50%. At constant δ, the λ_q^{mid} was relatively independent of the magnetic flux expansion in the range 10–40, leading to a strong reduction in the peak heat flux with increasing flux expansion because the λ_q^{div} increased linearly with flux expansion. Numerical

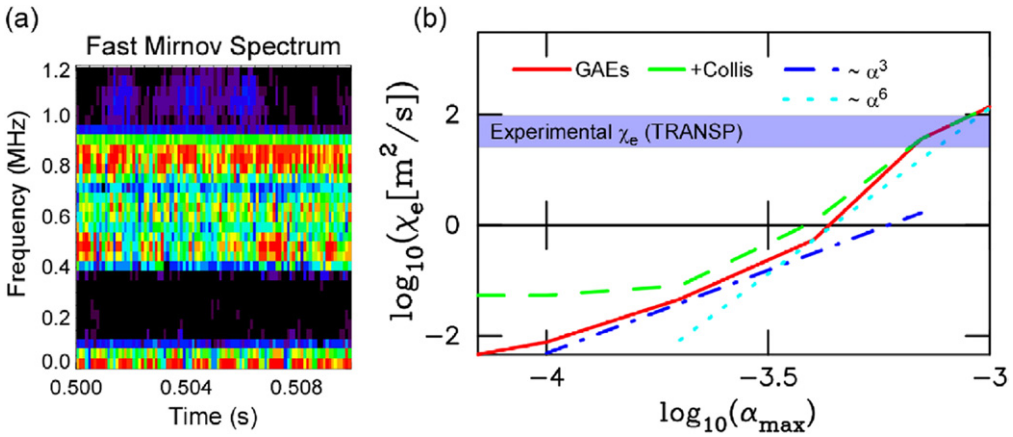

Figure 10. (*a*) Power spectrum from Mirnov magnetic pickup coils showing 'bursting' GAE behaviour in the frequency range 400–900 kHz. (*b*) Plot from ORBIT numerical calculations showing electron thermal transport induced by overlapping GAEs as a function of peak amplitude with (green) and without (red) collisions. Steady-state, rms measurements of mode amplitude $\sim 4 \times 10^{-4}$ under predicts TRANSP inferred experimental χ_e by a factor of ~4–10; however, strong dependence of χ_e on amplitude ($\sim\alpha^3$, $\sim\alpha^6$) indicates transport dominated by a maximum amplitude of bursting modes.

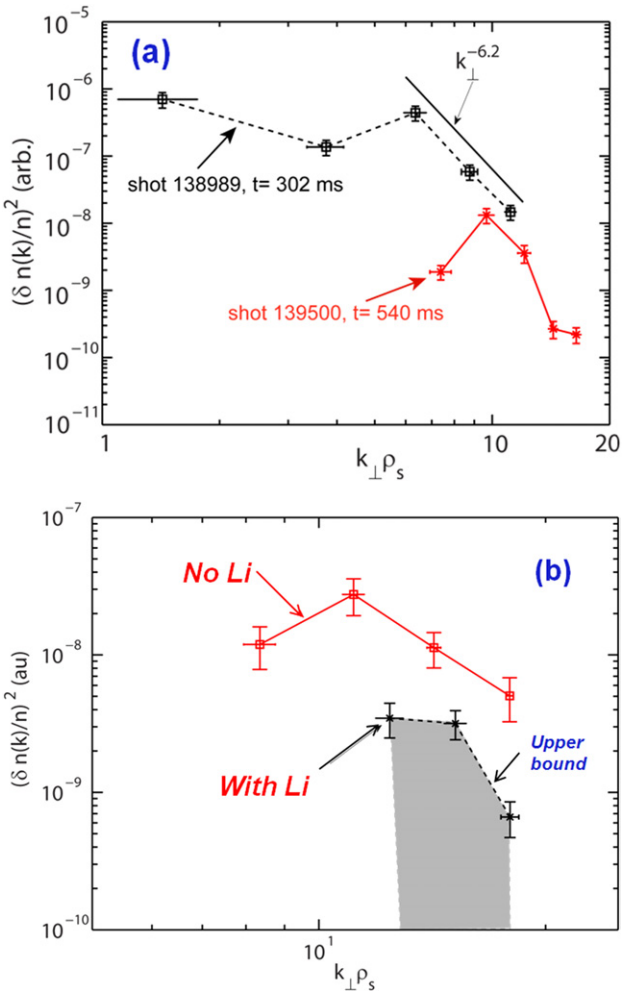

Figure 11. (*a*) The measured normalized k spectra in a beam-heated L-mode plasma (shot 138989) at $r/a \approx 0.77$ and in a beam-heated H-mode plasma (shot 139500) at $r/a \approx 0.85$. Both discharges have $I_p = 0.9$ MA, $B_T = 4.5$ kG and neutral-beam power of 2 MW. (*b*) The measured k spectra of normalized density fluctuations show a large reduction in the high-k turbulence power for the discharge that benefitted from lithium conditioning.

simulations [29] using a reduced turbulence model suggest that some of the observed scaling of $\lambda_q^{\rm mid}$ with $P_{\rm NBI}$ and I_p is due to intermittent convection spanning the whole separatrix.

Externally imposed non-axisymmetric magnetic perturbations have been observed to alter divertor heat and particle flux profiles. Even before the application of the 3D fields, multiple local peaks or striations were found in the divertor profiles of some discharges, characteristic of strike point splitting or a 'magnetic lobe' structure. These peaks are thought to be due to intrinsic error fields. The applied 3D fields substantially augmented these striations, amplifying the local peaks and valleys. The radial location and spacing of the striations are qualitatively consistent with vacuum field tracing [30, 31].

4.2. 'Snowflake' divertor (SFD) configuration development

The compact geometry of the ST divertor and the requirement of low density ($n_e/n_G \sim 0.55$–0.7, where n_G is the Greenwald density limit) operation for high neutral-beam current drive efficiency define a unique edge plasma regime which will place greater demands for handling the divertor and first-wall particle and heat fluxes. To address this need, a novel divertor configuration, called the SFD, has been tested on NSTX. The SFD uses a second-order X-point created by bringing close to each other two neighbouring first-order X-points. Experiments conducted on NSTX which obtained a SFD plasma configuration with just two divertor coils (figure 14) for periods of hundreds of milliseconds have confirmed many of its predicted benefits [32]. When compared with a similar medium triangularity ($\delta = 0.5 - 0.65$) standard divertor discharge in NSTX, the SFD maintained H-mode properties ($H_{98y,2} \sim 1$) without any degradation of stored energy and confinement. Divertor heat flux profiles showed a large reduction in peak heat flux during the SFD periods. Divertor radiation due to carbon impurity was significantly increased in the SFD. A large volume recombination region with $T_e \sim 1.5$ eV, $n_e > 3 \times 10^{20}$ m^{-3} developed, while ion flux to the divertor plate was reduced, suggesting an extended region of detachment in the divertor. As in previous divertor

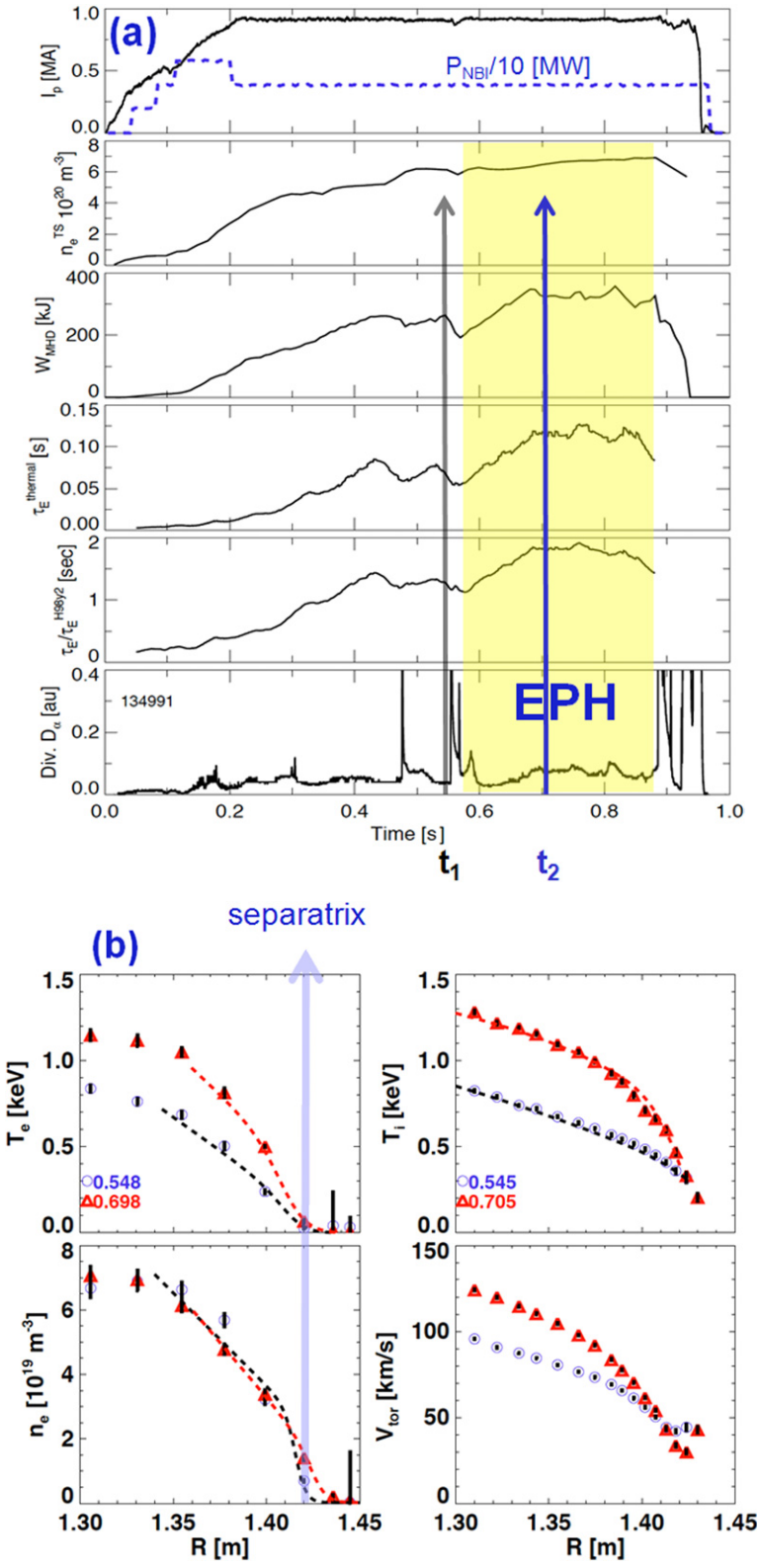

Figure 12. (*a*) Representative time traces and (*b*) profiles for a discharge which transitions to the 'enhanced-pedestal' (EP) H-mode. (*a*) Plasma current, neutral-beam power (dashed blue), line-average electron density, stored energy, thermal electron energy confinement time, ratio of the confinement time normalized to the ITER H98$y2$ scaling and the divertor D-alpha signal. During the H-mode phase of the discharge, an ELM triggers the EPH-mode at time t_1. The stored energy and the confinement time rapidly increase until time t_2, after which they are sustained for an additional nearly 200 ms. (*b*) Temperature, density and toroidal rotation profiles during the standard H-mode phase at time t_1 and during the EPH phase at time t_2. The dashed profiles represent fits to multiple profiles during the H-mode and EPH-mode phases.

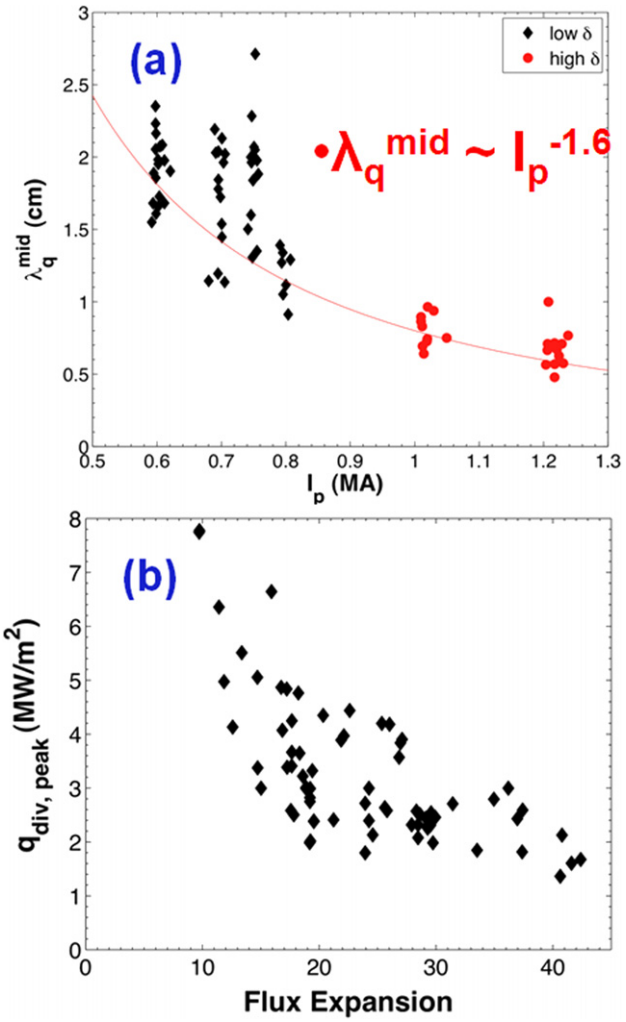

Figure 13. (*a*) Midplane heat flux width versus plasma current for low and high triangularity discharges (boronized, non-lithiated discharges) showing a strong decrease (proportional to $I_p^{-1.6}$) as the plasma current is increased. The use of lithium causes a further contraction of the SOL width. (*b*) The divertor heat flux plotted as a function of flux expansion shows it to be inversely proportional to flux expansion over a factor of 5 in range.

detachment experiments in NSTX [33], the core carbon density was reduced by up to 50%.

4.3. Lithium research

Evaporative Li coatings. Research into the effects of lithium-coated PFCs has been continued in NSTX using its two lithium evaporators (LITERs) [32, 34]. The evaporation of lithium onto the lower divertor, at total evaporation rates from 16 to 50 mg min^{-1}, for 10 or 8 min before each shot has obviated the need for pre-shot helium glow-discharge cleaning (HeGDC). Even relatively thin lithium coatings (typically 200–300 mg lithium deposited over roughly 2 m^2) significantly reduced the density in the early part of discharges, produced earlier H-mode transitions, and increased the electron temperature, electron stored energy and confinement time. H-mode discharges have been obtained with only 1 MW NBI (1.8 MW total power). At all power levels, as the lithium deposition increased, the discharges became increasingly ELM-free, and finally, fully ELM-free. The discharge pulse length has been increased with a combination of lithium conditioning, $n = 3$ error-field correction and $n = 1$ RWM feedback. Emission from O V and the ratio of O V to C III line emission decreased.

Lithium wall coatings reduced the recycling of the hydrogenic plasma component at the walls, as evidenced by a reduction in the overall D_α line emission, although the deuterium gas fuelling was often increased to maintain the density high enough to avoid locked modes developing during the early current ramp. The change in recycling relaxed the edge density profile gradients, as shown in figure 15. The maximum gradient in the edge T_e profile was largely unaffected, but the steep T_e gradients extended radially inwards by several cm following lithium coatings. Consequently, the pressure profile width and pedestal height increased substantially [35, 36]. Analysis with the edge stability code ELITE (figure 15) shows that pre-lithium discharges are close to the kink/peeling stability boundary, whereas the discharges that benefitted from the lithium coatings are within the stable region.

The improvement in electron stored energy occurred as a result of a broadening of the electron temperature profile, as shown in figure 16 [37]. The transport analysis code TRANSP [38] shows that the electron thermal transport in the outer region of the plasma is progressively reduced as lithium deposition increases [34]. The thermal ion confinement remains close to the neoclassical level both with and without lithium, although the fast-ion contribution to total energy increases as a result of the higher average electron temperature. With improvements in confinement and suppression of ELMs, there was a significant secular increase in the effective ion charge Z_{eff} and the radiated power in H-mode plasmas as a result of increases in the carbon and medium-Z metallic impurities. Lithium itself remained at a very low level in the plasma core, <0.1%.

Liquid lithium divertor (LLD). A LLD assembly was installed recently on the outer part of the lower divertor of NSTX [33]. The LLD consists of four plates, each spanning 80° toroidally, forming an annulus 0.22 m wide centred at a major radius of 0.75 m. The plasma-facing surface of the plates is flush with the surrounding graphite PFC tiles and consists of a 0.17 mm thick layer of molybdenum with 45% porosity, plasma sprayed on a protective barrier of 0.25 mm stainless steel, that is bonded to a 1.9 cm thick copper substrate. The plates were heated by embedded electric heaters or by heated compressed air passing through an embedded pipe. Lithium was applied to the LLD, and simultaneously to the surrounding graphite PFCs also, using the LITER system. With the LLD at initial temperatures in the range from 50 to 300 °C, the amount of gas fuelling required to prevent locked modes during plasma start-up and to maintain reproducible discharges, both indicators of the overall PFC-pumping ability, was similar to that for solid lithium coatings on graphite. After applying a fresh lithium coating 500–1000 nm thick on both the graphite tiles and the LLD, pumping by the lithium, as indicated by maintaining ELM-free H-modes with lower edge density and higher edge temperature, persisted only for two–three standard discharges (each ~1 s in duration) with the outer strike point on either the graphite inner divertor or the LLD. However, the

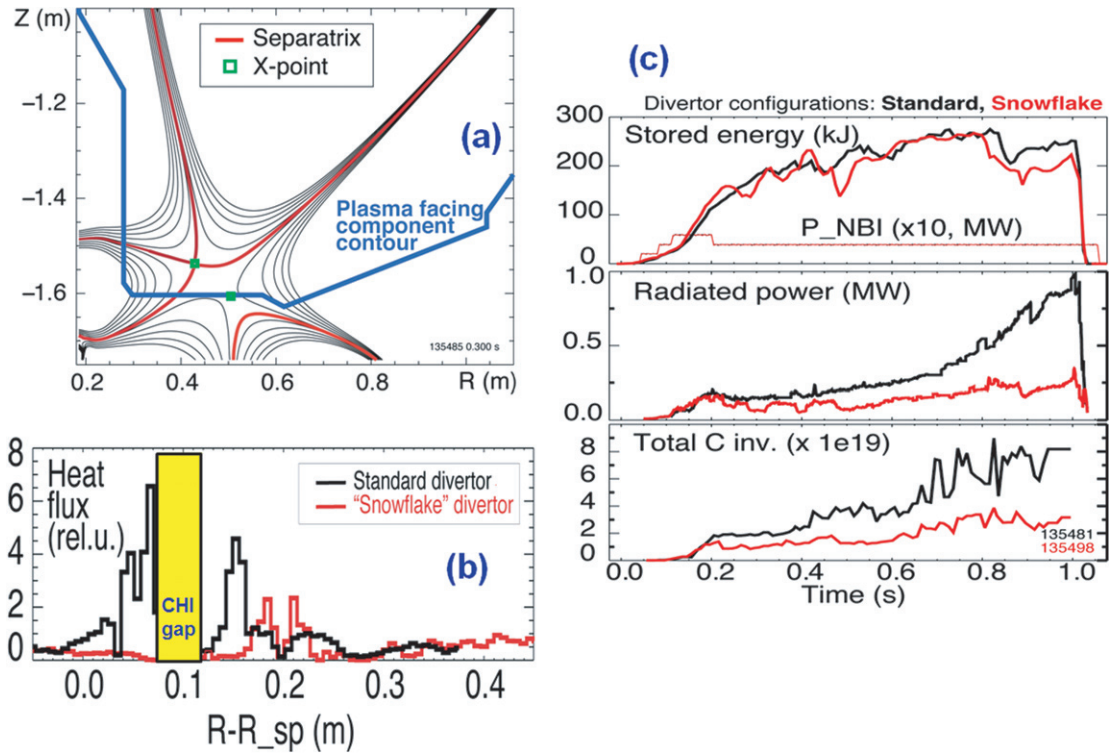

Figure 14. (*a*) The poloidal flux shape of a SFD configuration in NSTX; (*b*) comparison of the divertor heat flux profile for a snowflake configuration (red) with that of a standard divertor (black); (*c*) comparison of the stored energy, radiated power and total carbon inventory in the discharge for the snowflake and standard configurations.

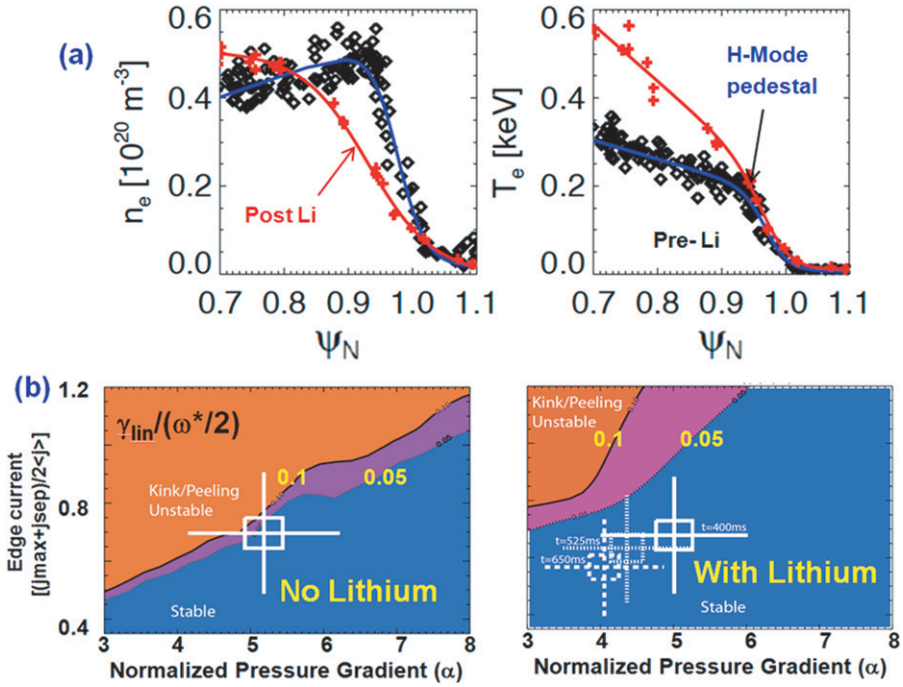

Figure 15. (*a*) The electron density and electron temperature profiles near the H-mode pedestal region for discharges with (red) and without (black) the use of lithium evaporative coatings. (*b*) Colour contours of the ratio of linear mode growth rate to diamagnetic drift frequency, obtained from ELITE code calculations. The discharge without lithium is close to the kink/peeling stability boundary but that boundary recedes with lithium applied.

persistence of lithium pumping increased to ∼100 discharges after more than 260 g of lithium had been evaporated onto the lower PFCs, filling the porous molybdenum surface of the LLD to ∼35% of its nominal capacity.

Diffusive Li deposition. In order to extend lithium coverage to a larger fraction of the NSTX PFCs, a new method was tested in which the LITERs evaporated lithium into low pressure helium gas. The mean free path of Li atoms in He was

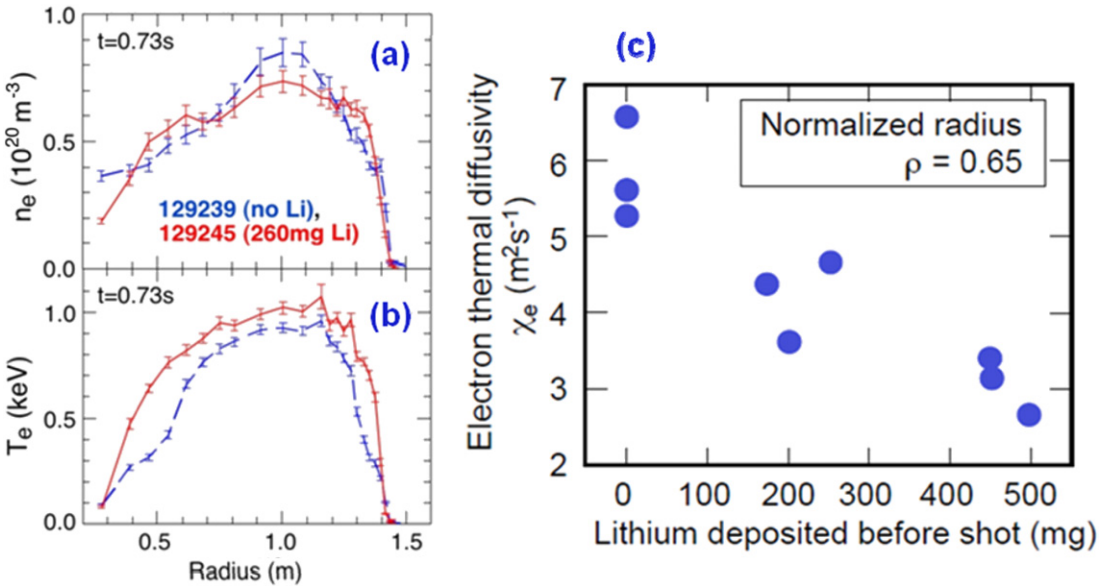

Figure 16. Comparison of the electron density and electron temperature profiles over the entire radius of the plasma for discharges without (blue) and with (red) lithium applied; (*b*) results from TRANSP analysis confirm that the electron thermal transport in the outer region is progressively reduced by lithium coatings.

varied by changing the helium pressure to produce a diffusive coating of the upper vessel, midplane and regions not in the line of sight to one of the LITERs. Monte Carlo modelling was used to derive a sequence of helium pressures to vary the lithium mean free path for optimal uniformity of lithium coverage of the PFCs. The increased lithium coverage of the vessel, which was evident in 2D camera images of Li II 5485 Å line emission from the plasma chamber, resulted in strong wall pumping and necessitated the increase in deuterium fuelling to very high levels [39].

Deuterium retention during and after plasma discharges. The processes governing deuterium retention by graphite and lithium-coated graphite PFCs were investigated in dedicated experiments involving measurements of the dynamic gas balance and analysis of the surface composition. These experiments were carried out using the LITER evaporators to deposit lithium on graphite divertor plates. In plasmas heated by NBI, the deuterium retention by the lithium-coated graphite was ∼93%, but the uncoated graphite retained somewhat less, ∼87%. Both with and without lithium, the retained deuterium was released as gas on timescales ranging from seconds to weeks or longer.

5. Wave–particle interactions in plasmas

5.1. Improved high harmonic fast-wave heating performance and understanding

The NSTX high-harmonic fast-wave (HHFW) system is designed both to heat electrons and to ramp-up and sustain plasma current non-inductively. The system consists of a twelve-element antenna fed by six power amplifiers operating at 30 MHz with total available power of 6 MW [40]. The phasing of RF waves between adjacent straps controls the wavenumber parallel to the magnetic field of the waves coupled to the plasma. Recent modifications of the antenna have increased the maximum arc-free power coupled to the plasma. A record central electron temperature T_e = 6.2 keV was achieved in helium L-mode plasmas with P_{RF} = 2.7 MW, representing a 30% increase in heating efficiency ($dT_e(0)/dP_{RF}$) compared with previous results. Moreover, a central $T_e > 3.5$ keV was sustained with P_{RF} = 2.7 MW for 0.3 s, much longer than previously achieved.

For waves launched with $k_\phi = -13\,m^{-1}$, the measured rate of rise in the plasma energy during the RF pulse indicates that about one third of the RF power is lost before it can couple to the plasma inside the separatrix of I_p = 1 MA, $B_T(0)$ = 0.55 T HHFW+NBI H-mode discharges, and this loss increases to about two-thirds for $k_\phi = -8\,m^{-1}$. While a parametric-decay instability may account for some of this RF power loss, it appears that there is a significant additional fast-wave power loss occurring in these H-mode discharges. Evidence for this is provided by visible and infrared camera measurements, as shown in figure 17. The top three panels show colour camera images taken during three I_p = 1 MA, B_T = 0.55 T deuterium H-mode plasmas. The top image is from a plasma that had only 2 MW of NBI heating (shot 130609). The second and third images are from plasmas that had 2 MW of NBI heating, but also had 1.8 MW of $k_\phi = -8\,m^{-1}$ RF heating (shot 130621) and 1.9 MW $k_\phi = -13\,m^{-1}$ RF heating (shot 130608), respectively. The images in the second and third panels were taken at 0.335 s. The top image was taken at 0.350 s. A NBI-only background frame at 0.250 s in each shot was subtracted from each image to show differences in the image when HHFW power was applied. When RF heating was applied, power flowed along the magnetic field lines onto the lower outer divertor plate. This flow became much more prominent for the case with $k_\phi = -8\,m^{-1}$ heating than for the case with $k_\phi = -13\,m^{-1}$ heating, in keeping with lower core heating efficiency at $k_\phi = -8\,m^{-1}$. Recently, dramatic evidence of the power densities associated with this interaction has been provided by infrared

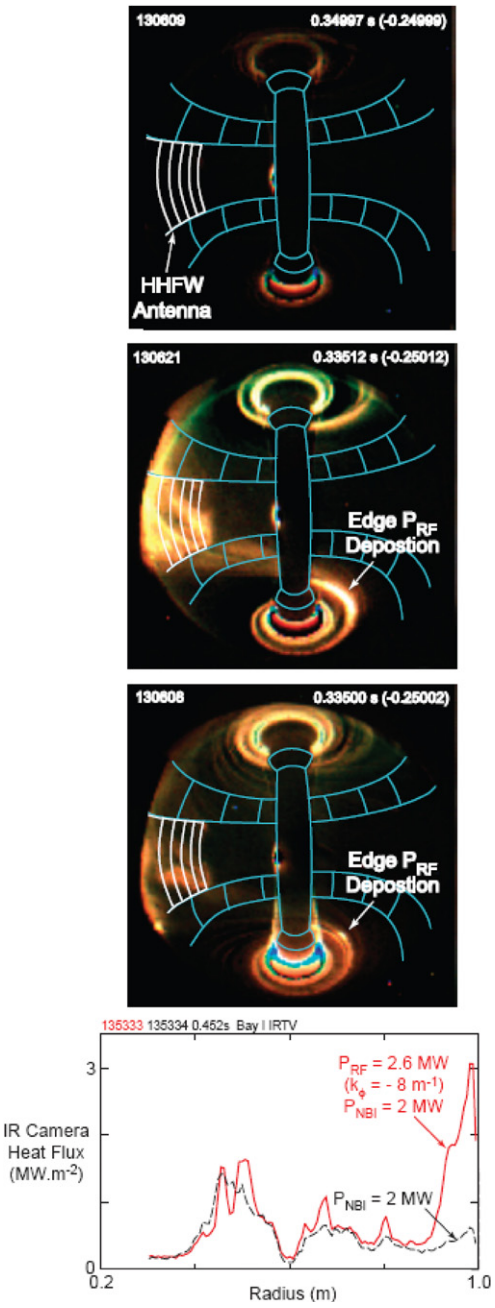

Figure 17. The three visible camera images are for $I_p = 1$ MA, $B_T(0) = 0.55$ T deuterium H-mode plasmas. The top image is for plasma with only 2 MW of NBI heating. The next two images are each for plasmas with 2 MW of NBI heating plus 1.8 MW of $k_\phi = -8\,\mathrm{m}^{-1}$ HHFW heating and 1.9 MW $k_\phi = -13\,\mathrm{m}^{-1}$ heating, respectively. The bottom panel shows the heat flux versus major radius measured by an IR camera viewing the lower divertor plate during two $I_p = 800$ kA, $B_T(0) = 0.45$ T deuterium H-mode plasmas, one (black dashed) with 2 MW of NBI only and the other with 2 MW of NBI and 2.6 MW of $k_\phi = -8\,\mathrm{m}^{-1}$ HHFW heating (red solid).

camera measurements of the lower divertor plates. Figure 17 (bottom panel) shows a plot of the heat flux versus major radius for two H-mode discharges, one with 2 MW of NBI, and the other with 2 MW of NBI plus 2.6 MW of $k_\phi = -8\,\mathrm{m}^{-1}$ RF heating. These discharges had a similar shape to those in the top three panels. The heat flux to the lower outer divertor plate increased by about a factor of 6 at $R = 0.98$ m, to 3 MW m^{-2} when RF heating was applied.

Progress was made in understanding the interaction of RF with the fast ions from NB injection. The FIDA diagnostic [41] measured changes in the fast-ion density during HHFW heating [42]. An increase by a factor $\geqslant 2$ was measured near the magnetic axis (corresponding to the seventh and eighth deuterium cyclotron harmonics), gradually decreasing near the plasma edge (11th harmonic). Significant differences are observed between the measured fast-ion profiles and calculations from the CQL3D Fokker–Planck code [43]. The peak in the predicted fast-ion density is three times higher and much more localized than the measured value. The cause of this discrepancy is likely to be the zero ion-banana-width approximation used in CQL3D, whereas this parameter is large on NSTX, in the range 10–15 cm. Finite banana-width effects are being incorporated into CQL3D and simulations with the ORBIT-RF [43] finite-orbit Monte Carlo code coupled with the full wave code AORSA [44] are in progress to improve their predictive capability for fast-ion interactions with the HHFW in NSTX.

5.2. Study of Alfvénic instabilities and associated fast-ion transport

NSTX routinely operates with $V_{\mathrm{fast}}/V_{\mathrm{Alfven}}$ (V_{fast} is the typical velocity of non-thermal ions) in the range 1–5, comparable to expectations for ITER. This provides a large drive for Alfvénic eigenmodes (AEs). Recent experiments have mainly focused on the interactions between the fast ions from NBI and toroidal Alfvén eigenmodes (TAEs) and energetic-particle modes (EPMs). These interactions are thought to be the main fast-ion loss mechanism threatening burning-plasma devices such as ITER [45]. Fast-ion losses induced by bursting TAE *avalanches* [46] have been extensively documented in L-mode plasmas [47]. It was found that TAEs can deplete up to ~30% of the fast-ion population over a significant portion of the minor radius. The losses increased with the mode amplitude [46]. In contrast, there is no clear evidence of losses associated with higher frequency modes, which include global Alfvén eigenmodes (GAEs) and compressional Alfvén eigenmodes (CAEs) extending up to ~2 MHz. However, a correlation between GAE bursts and TAE avalanches has been observed, suggesting that GAEs may cause a redistribution of fast ions that, in turn, can trigger the avalanches [48]. Figure 18(*a*) shows the TAE spectrum and the associated drop in neutron rate. An examination of the fast-ion profile before and after the TAE event around 360 ms (figure 18(*b*)) shows that the fast-ion profile is depleted over the entire radius and that the effect is not local.

The fast-ion losses caused by TAE avalanches have been successfully modelled [46, 49] through the ORBIT code [50], using the mode structures calculated by the NOVA code [51]. The mode structures are re-scaled to match that measured by reflectometers. Figure 19 shows that the calculated fast-ion loss increases sharply with the TAE amplitude and that the measured neutron drop is consistent with the ORBIT calculations (note that the modelling was for a different discharge from the one shown in figure 18(*b*)).

Future experiments will extend TAE studies to H-mode scenarios. In parallel, validation of self-consistent, non-linear

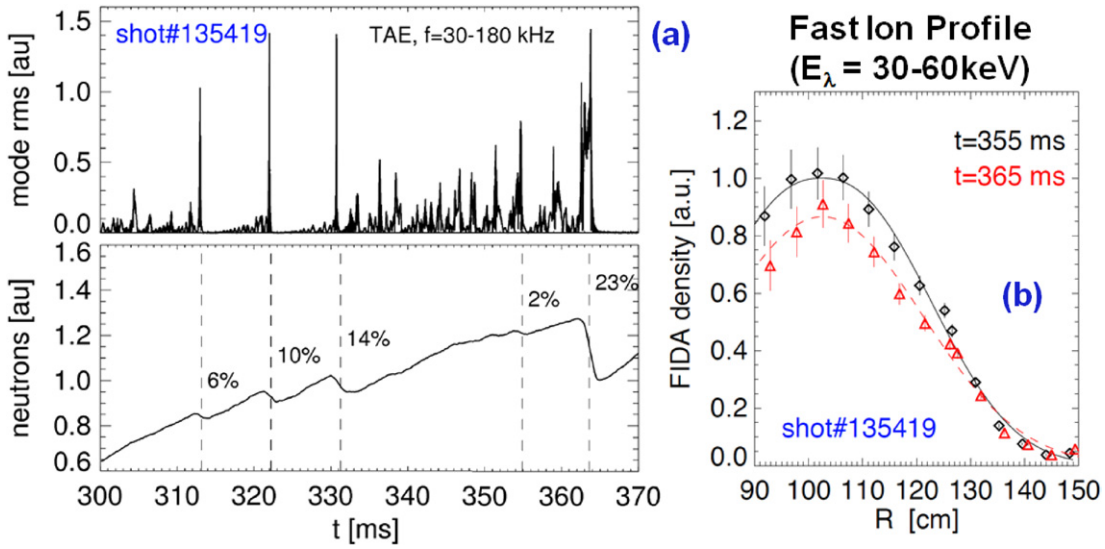

Figure 18. (*a*) Bursts of TAE activity (top panel) between 300 and 370 ms are associated with drops in the DD neutron rate (bottom panel); (*b*) fast-ion profiles before and after the TAE event at 360 ms show a depletion of the fast-ion density.

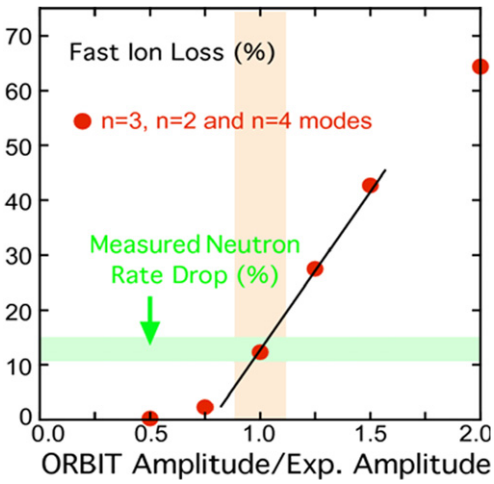

Figure 19. ORBIT code calculations of fast-ion loss versus TAE mode amplitude normalized to the experimental value.

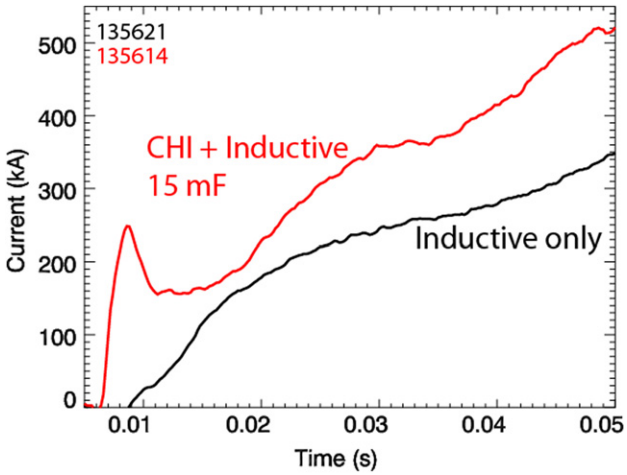

Figure 20. Plasma current traces during plasma initiation from discharges started with (red) and without (black) CHI. Both use the same pre-programmed inductive flux.

codes (e.g. M3D-K, [52]) is being pursued to improve the predictive capability of AE dynamics, including associated fast-ion transport and non-linear phenomena, towards next generation devices and ITER.

6. Plasma start-up without reliance on a central solenoid

In the ST configuration there is little room for a central solenoid to initiate and sustain the plasma by induction, as is usually done in a conventional tokamak with higher aspect ratio. Although NSTX is equipped with a central solenoid, it is also exploring several approaches to starting and sustaining plasmas in the ST without relying solely on it. The primary non-inductive start-up technique in NSTX is coaxial helicity injection (CHI) which uses a power supply to create a discharge carrying poloidal current between the inner and outer divertor annuli which are insulated from each other [53]. In the presence of a toroidal field, the current carried by the plasma, which flows along magnetic field lines, develops a strong toroidal component. Through the process of magnetic reconnection, that toroidal current can be transferred from the open magnetic field lines connecting the divertor electrodes to the closed, nested flux surfaces of standard tokamak equilibrium.

Previously, up to 50 kA of toroidal plasma current produced by CHI was successfully coupled to inductive ramp-up in NSTX. When heated with NBI, these discharges achieved plasma temperatures over 0.8 keV and transitioned to the H-mode, demonstrating the compatibility of CHI start-up with standard plasma operation. However, in previous experiments, the CHI current that could be successfully coupled was limited by impurity production from the CHI electrodes and the occurrence of absorber arcs (i.e. parasitic discharges across the insulating gap in the upper divertor). Extensive conditioning of the divertor plates that serve as the electrodes for the

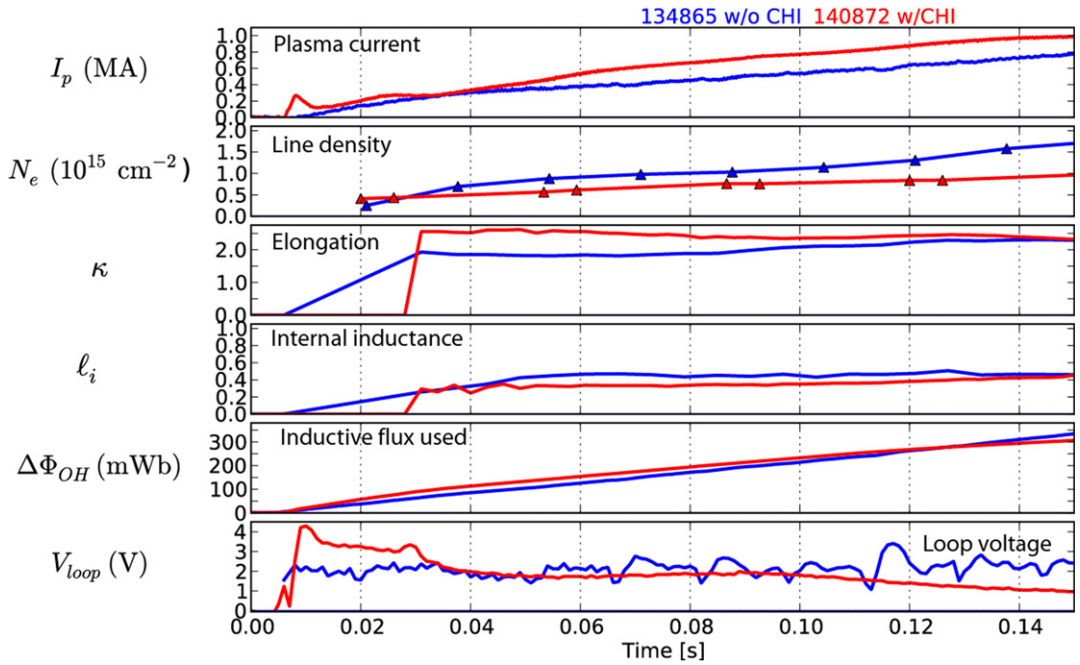

Figure 21. Comparison of a discharge initiated using CHI start-up and ramped-up using induction (red) with a standard inductive-only discharge (blue). Shown are the plasma current, electron line density, plasma elongation, plasma internal inductance, the change in flux in the central solenoid and the loop voltage. Despite having a much lower density and faster current ramp-rate, the CHI started discharge is free of MHD activity. The higher density and slower ramp rates are required for the inductive-only discharge to avoid reconnection events.

CHI discharge has now greatly reduced impurity production during CHI [54]. Further, by energizing, for the first time, the axisymmetric poloidal field coils located near the upper divertor in NSTX, the absorber arcs have been delayed or suppressed. These improvements have increased the current at the hand-off from CHI to induction to nearly 200 kA. Later in the inductive ramp-up, the discharges with CHI applied reached significantly higher plasma current than discharges with only the inductive loop voltage applied. For example, in discharges with identical programming of the central solenoid current, the plasma current at $t = 50$ ms (the CHI is applied only to $t \approx 15$ ms) increased from 340 kA with induction only to 520 kA with CHI (figure 20). This represents a poloidal flux saving equivalent to 180 kA of plasma current which is ~25% of the flat-top current of 700 kA typical of long-pulse scenarios on NSTX. The most recent experiments [53] in which CHI initiation was followed by inductive ramp-up, produced final currents exceeding 1 MA using only 0.28 Wb of the 0.33 Wb of inductive flux available from a uni-directional swing of the central solenoid. This is the highest current produced in NSTX using this amount of central solenoid flux, and is a significant improvement over the 800 kA previously achieved using all of the flux from a single swing of the central solenoid, as described in [54]. As shown in figure 21, these plasmas have both a very high elongation of $\kappa \approx 2.6$ and, as a result of the hollow electron temperature profile and rapid inductive ramp, very low internal inductance $l_i \approx 0.3$ from the start of the discharge. Finally, these plasmas are relatively free of MHD activity despite having low density, which has previously been associated with increased instability during normal inductive start-up. The comparison of a CHI started discharge with an inductive-only discharge is shown in figure 21. Simulations with the code TSC [55] suggest that these targets should be capable of reaching a high fraction of neutral-beam driven current. Thus, the 2010 campaign has not only significantly improved CHI start-up capability, but also produced the type of plasmas that are needed to meet the objectives of the non-inductive start-up and ramp-up program in NSTX.

7. The development of integrated high-performance scenarios

A major goal for NSTX research is the achievement of high-β discharges which can be maintained non-inductively for long pulses, eventually extending to several relaxation times of the current profile. To achieve this, it will be necessary to maximize the bootstrap current, and the current driven by the NB injection. Significant progress has now been made in increasing the bootstrap current and the pulse length in NBI-heated H-mode plasmas by a combination of techniques [56]. The first of these has been to raise the plasma elongation, κ, which increases the poloidal-beta β_P at fixed normalized-beta β_N. Highly reliable scenarios with high-κ, and high-β_N that have 60–65% non-inductive current drive fraction have now been produced as shown in the black trace in figure 22. This $B_T = 0.48$ T discharge achieved a maximum $\beta_P \approx 1.8$ and $\beta_P > 1.6$ for 0.5 s, with ~50% of the toroidal current driven by the plasma pressure, and ~20% by the neutral beams. It was limited in duration by the heating of the TF coil. By decreasing the toroidal field to $B_T = 0.38$ T, the TF pulse was extended (blue trace) although the coil heating still limited the discharge length. Confinement in these discharges was increased using lithium wall coating, and routinely achieved a global energy confinement time enhancement $H_{98y,2} = 1$ relative to the ITER-98$_{y,2}$ H-mode scaling expression [56]. Both $n = 3$ error-field correction and $n = 1$ feedback

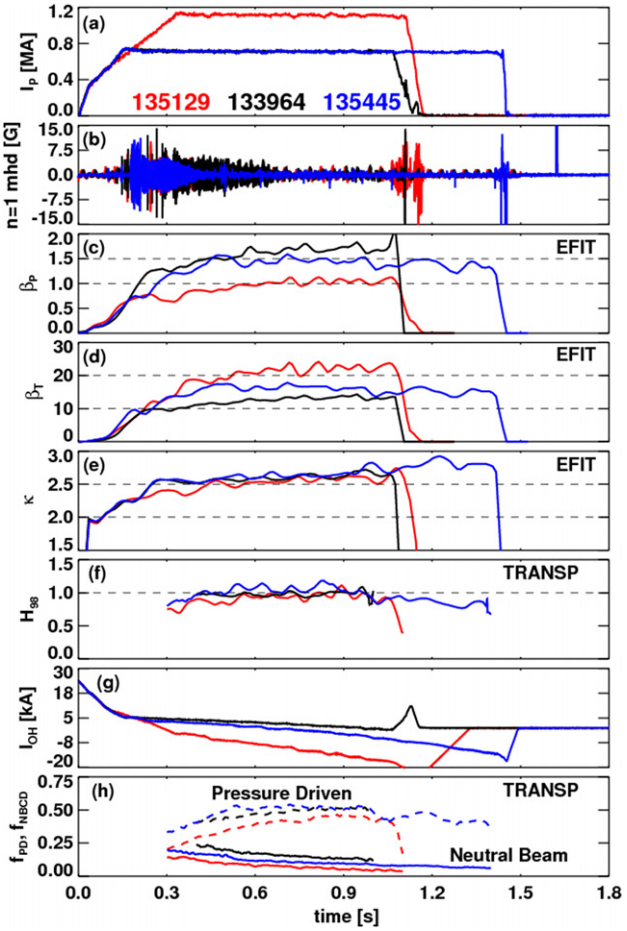

Figure 22. Representative discharge parameters for high-elongation discharges designed to maximize the non-inductive fraction (black), the pulse length (blue), and toroidal beta, β_T (red).

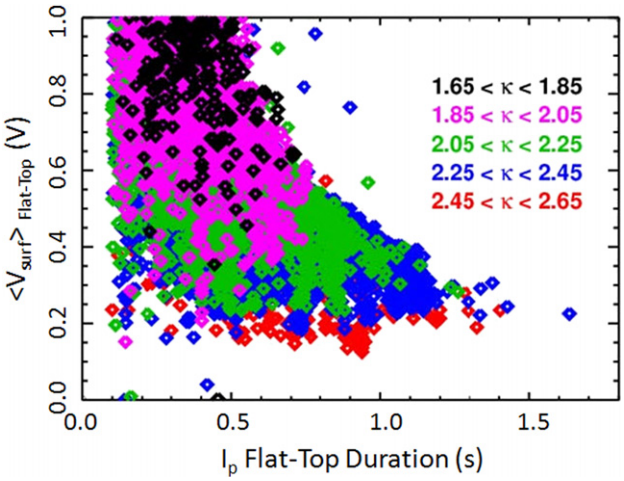

Figure 23. Pulse-averaged surface loop voltage versus the current flat-top duration, sorted by the plasma boundary elongation. Increases in the elongation have led to a factor of ∼2 reduction in the surface voltage.

were used to maintain high plasma rotation and suppress potential RWMs. These discharges were then extended to higher normalized current by further reducing the toroidal field and increasing the plasma current, as shown in the red trace in figure 22. This allowed sustained values of toroidal beta, β_T, approaching 25%. These higher β_T cases had non-inductive current fractions of almost 50%. Also noteworthy are the very high values of the parameter $\beta_N/l_i \approx 13$ (% m T MA^{-1}), compared with ∼4 in conventional tokamaks. These discharges provide a test of MHD control techniques at parameters relevant to a future ST-based component test facility for fusion power development. The reliability of these high β_N/l_i scenarios has been shown to improve when the feedback control with $n = 1$ mode detection using both B_P and B_R sensors near the outboard midplane of the plasma was utilized for the RWM control [1].

As shown in figure 23, discharges with loop voltages averaged over the plasma current flat-top of only about 130 mV have been sustained for 0.9 s. These discharges had the lowest flux consumption of any NSTX H-mode plasma to date: at the end of the toroidal field pulse, again imposed by the coil heating, most of these discharges had used only half of the available transformer flux of 0.7 Wb. These high-κ, high-β scenarios, which are the culmination of a continuing effort to achieve sustained high-elongation operation, represent a substantial extension of the operational space available in NSTX and will serve as the basis for the NSTX upgrade and also for future ST devices.

NSTX has also benefited from substantial improvements in plasma shape control in the past two years [57, 58]. Controllers have been developed to regulate both the radius of the outer strikepoint (on the lower horizontal divertor target) and the height of the inner strikepoint (on the lower vertical target). These controllers were used to provide the basic configuration for studies with the LLD and to create SFDs. Controllers were also developed to regulate the outer strikepoint radius and X-point height, and the relative merits of these two control strategies remain under study. Finally, initial studies of the effect of the plasma squareness on transport and global stability have begun.

8. Summary

Over the last two years, the low aspect ratio NSTX has explored physics issues critical to both toroidal confinement physics and ITER. Experiments have made extensive use of both lithium coatings for wall conditioning and external non-axisymmetric field correction to reliably produce high-performance discharges with non-inductive current fractions of up to 0.70, extending to 1.7s in duration. A new 'enhanced-pedestal' H-mode regime has achieved energy confinement substantially above the ITER H-mode scaling. Measurements of the divertor heat flux have characterized the dominant scalings and revealed structures generated by field errors. To reduce divertor heat flux, a novel divertor configuration, called the SFD has been tested.

The external error-field correction coils have contributed to improved understanding of both RWM and NTM physics and have been used to trigger ELMs with high reliability. Research in NSTX has shown that kinetic effects are important for determining the plasma rotation required for RWM stability. The study of error-field penetration phenomena, including mode locking, driven by external non-axisymmetric fields has been extended to high-β discharges. ELM pacing

with periodic non-axisymmetric field pulses has been shown to be effective at preventing impurity accumulation while retaining the high H-mode confinement.

Measurements have been made of the power threshold for the L-mode to H-mode transition in RF-heated helium and deuterium plasmas. The relatively small difference in the power threshold suggests that operation in helium may provide access to the H-mode in the early non-nuclear phase of ITER operation. Experiments have investigated the dependences of the momentum diffusivity and pinch velocity on collisionality which are important for predicting the plasma rotation in ITER.

Density fluctuation measurements have shown that the lower-k turbulence is quite different in L- and H-mode plasmas, whereas the higher-k turbulence is largely unaffected. Results from a new fast-ion diagnostic show a depletion of the fast-ion density introduced by NBI over a broad spatial region caused by bursts of toroidicity-induced Alfvén eigenmodes and EPMs.

A reduction in the required central solenoid flux has been realized in NSTX when discharges initiated by coaxial helicity injection were ramped in current using induction. This represents significant progress towards the goal of non-inductive start-up and sustainment in NSTX.

Acknowledgments

This paper has been authored by Princeton University and collaborators under contract number(s) DE-AC02-09CH11466 and DE-FG02-99ER54519 AM08 with the US Department of Energy. The publisher, by accepting this paper for publication, acknowledges that the United States Government retains a non-exclusive, paid-up, irrevocable, world-wide license to publish or reproduce the published form of this manuscript, or allow others to do so, for United States Government purposes.

References

[1] Sabbagh S.A. *et al* 2010 *Proc. 23rd Int. Conf. on Fusion Energy 2010 (Daejeon, Korea, 2010)* (Vienna: IAEA) CD-ROM file EXS/5-5 and http://www-naweb.iaea.org/napc/physics/FEC/FEC2010/html/index.htm
[2] Sabbagh S.A. *et al* 2010 *Nucl. Fusion* **50** 025020
[3] Menard J.E. *et al* 2010 *Nucl. Fusion* **50** 045008
[4] Gerhardt S.P. *et al* 2010 *Plasma Phys. Control. Fusion* **52** 104003
[5] Katsuro-Hopkins O.N., Sabbagh, S.A. and Bialek J.M. 2009 *Proc. 48th IEEE Conf. on Decision and Control. (Shanghai, China)* p 309
[6] Berkery J.F. *et al* 2010 *Phys. Rev. Lett.* **104** 035003
[7] Garofalo A.M. *et al* 2007 *Nucl. Fusion* **47** 1121
[8] Berkery J.F. *et al* 2010 *Phys. Plasmas* **17** 082504
[9] Hu B., Betti R. and Manickam J. 2005 *Phys. Plasmas* **12** 057301
[10] Reimerdes H. *et al* 2004 *Phys. Rev. Lett.* **93** 135002
[11] Park J-K. *et al* 2009 *Phys. Plasmas* **16** 056115
[12] Buttery R.J. *et al* 1999 *Nucl. Fusion* **38** 1827
[13] Buttery R.J. *et al* 2011 The impact of 3-D fields on tearing mode stability in H-modes *Nucl. Fusion* at press
[14] La Haye R.J. *et al* 2010 *Phys. Plasmas* **17** 056110
[15] Canik J.M. *et al* 2010 *Phys. Rev. Lett.* **104** 045001
[16] Canik J.M. *et al* 2010 *Proc. 23rd Int. Conf. on Fusion Energy 2010 (Daejeon, Korea, 2010)* (Vienna: IAEA) CD-ROM file EXC/8-1 and http://www-naweb.iaea.org/napc/physics/FEC/FEC2010/html/index.htm
[17] Gerhardt S.P. *et al* 2010 *Nucl. Fusion* **50** 064015
[18] Chang C.S. *et al* 2004 *Phys. Plasmas* **11** 2649
[19] Kaye S.M. *et al* 2011 L–H threshold studies in NSTX *Nucl. Fusion* at press
[20] Solomon W.M. *et al* 2010 *Phys. Plasmas* **17** 056108
[21] Stutman D. *et al* 2009 *Phys. Rev. Lett.* **102** 115002
[22] Mazzucato E. 2006 *Plasma Phys. Control. Fusion* **48** 1749
[23] Smith D.R. *et al* 2008 *Rev. Sci. Instrum.* **79** 123501
[24] Mazzucato E. *et al* 2008 *Phys. Rev. Lett.* **101** 075001
[25] Smith D.R. *et al* 2009 *Phys. Plasmas* **16** 112507
[26] Smith D.R. *et al* 2009 *Phys. Rev. Lett.* **102** 225005
[27] Maingi R. *et al* 2010 *Phys. Rev. Lett.* **105** 135004
[28] Gray T.K. *et al* 2010 *Proc. 23rd Int. Conf. on Fusion Energy 2010 (Daejeon, Korea, 2010)* (Vienna: IAEA) CD-ROM file EXD/P3-13 and http://www-naweb.iaea.org/napc/physics/FEC/FEC2010/html/index.htm
[29] Myra J.R. *et al* 2010 *J. Nucl. Mater.* at press (doi:10.1016/j.jnucmat.2010.10.030)
[30] Ahn J.-W. *et al* 2010 *Nucl. Fusion* **50** 045010
[31] Ahn J.-W. *et al* 2010 *Proc. 23rd Int. Conf. on Fusion Energy 2010 (Daejeon, Korea, 2010)* (Vienna: IAEA) CD-ROM file EXD/P3-01 and http://www-naweb.iaea.org/napc/physics/FEC/FEC2010/html/index.htm
[32] Soukhanovskii V. *et al* 2010 *Proc. 23rd Int. Conf. on Fusion Energy 2010 (Daejeon, Korea, 2010)* (Vienna: IAEA) CD-ROM file EXD/P3-32 and http://www-naweb.iaea.org/napc/physics/FEC/FEC2010/html/index.htm
[33] Soukhanovskii V.A. *et al* 2009 *Phys. Plasmas* **16** 022501
[34] Kugel H.W. *et al* 2010 *Proc. 23rd Int. Conf. on Fusion Energy 2010 (Daejeon, Korea, 2010)* (Vienna: IAEA) CD-ROM file FTP/3-6Ra and http://www-naweb.iaea.org/napc/physics/FEC/FEC2010/html/index.htm
[35] Maingi R. *et al* 2009 *Phys. Rev. Lett.* **103** 075001
[36] Maingi R. *et al* 2010 *Proc. 23rd Int. Conf. on Fusion Energy 2010 (Daejeon, Korea, 2010)* (Vienna: IAEA) CD-ROM file EXD/2-2 and http://www-naweb.iaea.org/napc/physics/FEC/FEC2010/html/index.htm
[37] Ding S. *et al* 2010 *Plasma Phys. Control. Fusion* **52** 015001
[38] Hawryluk R.J. *et al* 1980 An empirical approach to tokamak transport *Physics of Plasmas Close to Thermonuclear Conditions* vol. 1, ed B. Coppi *et al* (Brussels: CEC) pp 19–46
[39] Skinner C.H. *et al* 2010 *J. Nucl. Mater.* at press (doi:10.1016/j.jnucmat.2010.08.063)
[40] Taylor G. *et al* 2010 *Phys. Plasmas* **17** 056114
[41] Podestà M. *et al* 2008 *Rev. Sci. Instrum.* **79** 10E521
[42] Liu D. *et al* 2010 *Plasma Phys. Control. Fusion* **52** 025006
[43] Choi M. *et al* 2005 *Phys. Plasmas* **12** 072505
[44] Jaeger E.F. *et al* 2001 *Phys. Plasmas* **8** 1573
[45] Fasoli A. *et al* 2007 *Nucl. Fusion* **47** S264
[46] Fredrickson E. *et al* 2009 *Phys. Plasmas* **16** 122505
[47] Podestà M. *et al* 2009 *Phys. Plasmas* **16** 056104
[48] Fredrickson E. *et al* 2010 *Proc. 23rd Int. Conf. on Fusion Energy 2010 (Daejeon, Korea, 2010)* (Vienna: IAEA) CD-ROM file EXW/P7-06 and http://www-naweb.iaea.org/napc/physics/FEC/FEC2010/html/index.htm
[49] Podestà M. *et al* 2011 *Nucl. Fusion* **51** 063035
[50] White R. *et al* 1984 *Phys. Fluids* **27** 2455
[51] Cheng C. 1992 *Phys. Rep.* **211** 1
[52] Lang J. *et al* 2009 *Phys. Plasmas* **16** 102101
[53] Nelson B.A. *et al* 2011 *Nucl. Fusion* **51** 063008
[54] Raman R. *et al* 2010 *Phys. Rev. Lett.* **104** 095003
[55] Kessel C.E. *et al* 2005 *Nucl. Fusion* **45** 814
[56] Gerhardt S.P. *et al* 2011 Recent progress toward an advanced spherical torus operating point in NSTX *Nucl. Fusion* at press
[57] Kolemen E. *et al* 2010 *Proc. 23rd Int. Conf. on Fusion Energy 2010 (Daejeon, Korea, 2010)* (Vienna: IAEA) CD-ROM file EXD/P3-18 and http://www-naweb.iaea.org/napc/physics/FEC/FEC2010/html/index.htm
[58] Kolemen E. *et al* 2010 *Nucl. Fusion* **50** 105010